REPORT DOCUMENTATION PAGE

Form Approved OMB NO. 0704-0188

The public reporting burden for this collection of information is estimated to average 1 hour per response, including the time for reviewing instructions, searching existing data sources, gathering and maintaining the data needed, and completing and reviewing the collection of information. Send comments regarding this burden estimate or any other aspect of this collection of information, including suggesstions for reducing this burden, to Washington Headquarters Services, Directorate for Information Operations and Reports, 1215 Jefferson Davis Highway, Suite 1204, Arlington VA, 22202-4302. Respondents should be aware that notwithstanding any other provision of law, no person shall be subject to any oenalty for failing to comply with a collection of information if it does not display a currently valid OMB control number.
PLEASE DO NOT RETURN YOUR FORM TO THE ABOVE ADDRESS.

1. REPORT DATE (DD-MM-YYYY)	2. REPORT TYPE	3. DATES COVERED (From - To)
06-12-2015	Ph.D. Dissertation	-

4. TITLE AND SUBTITLE
An investigation of physics and control of flow passing a NACA 0015 in fully-reversed condition

5a. CONTRACT NUMBER
W911NF-12-2-0058

5b. GRANT NUMBER

5c. PROGRAM ELEMENT NUMBER
611102

6. AUTHORS
C. Clifford

5d. PROJECT NUMBER

5e. TASK NUMBER

5f. WORK UNIT NUMBER

7. PERFORMING ORGANIZATION NAMES AND ADDRESSES
Ohio State University
1960 Kenny Road

Columbus, OH 43210 -1016

8. PERFORMING ORGANIZATION REPORT NUMBER

9. SPONSORING/MONITORING AGENCY NAME(S) AND ADDRESS (ES)
U.S. Army Research Office
P.O. Box 12211
Research Triangle Park, NC 27709-2211

10. SPONSOR/MONITOR'S ACRONYM(S)
ARO

11. SPONSOR/MONITOR'S REPORT NUMBER(S)
62204-EG.7

12. DISTRIBUTION AVAILIBILITY STATEMENT
Approved for public release; distribution is unlimited.

13. SUPPLEMENTARY NOTES
The views, opinions and/or findings contained in this report are those of the author(s) and should not contrued as an official Department of the Army position, policy or decision, unless so designated by other documentation.

14. ABSTRACT
See the dissertation

15. SUBJECT TERMS
Flow control, rotorcraft flow, plasma actuators

16. SECURITY CLASSIFICATION OF:			17. LIMITATION OF ABSTRACT	15. NUMBER OF PAGES	19a. NAME OF RESPONSIBLE PERSON
a. REPORT	b. ABSTRACT	c. THIS PAGE			Mo Samimy
UU	UU	UU	UU		19b. TELEPHONE NUMBER 614-292-5012

Report Title

An investigation of physics and control of flow passing a NACA 0015 in fully-reversed condition

ABSTRACT

See the dissertation

An Investigation of Physics and Control of Flow Passing a NACA 0015 in Fully-Reversed Condition

Dissertation

Presented in Partial Fulfillment of the Requirements for the Degree Doctor of Philosophy in the Graduate School of The Ohio State University

By

Christopher J. Clifford, B.S.

Graduate Program in Mechanical Engineering

The Ohio State University

2015

Dissertation Committee:

Dr. Mo Samimy, Advisor

Dr. Igor Adamovich

Dr. Datta Gaitonde

Dr. James Gregory

Copyright © Christopher J. Clifford 2015.

This thesis is licensed under the

Creative Commons Attribution 4.0 International License.

To view a copy of this license, visit:

http://creativecommons.org/licenses/by/4.0/

or send a letter to:

Creative Commons

171 Second Street, Suite 300

San Francisco, California 94105

USA

Abstract

Flow control experiments were performed on a NACA 0015 airfoil in fully-reversed condition, which is anticipated to occur on the retreating blade side of advanced helicopters such as slowed-rotor compound rotorcraft. Control was achieved using **n**ano**s**econd **d**ielectric **b**arrier **d**ischarge (NS-DBD) plasma actuators. The Reynolds number based on a chord length of 203 mm was fixed at $5.0 \cdot 10^5$, corresponding to a freestream velocity of $\sim$38 m/s. Two angles of attack were considered: $\alpha = 0°$ and 15°, each of which is relevant to a particular implementation of slowed-rotor technology.

At $\alpha = 0°$, the flow resembles that of a flow behind a cylinder. A von Kármán vortex street formed in the wake where alternating vortex shedding occurred at a Strouhal number of 0.12. Excitation was performed using an NS-DBD on one side of the airfoil, with plasma formation just upstream of the separation line. However, there was no discernible influence upon the baseline behavior.

At $\alpha = 15°$, fully separated flow on the suction side extended well beyond the airfoil with naturally shed vortices at a Strouhal number of 0.19. Plasma actuation was evaluated at both the **a**erodynamic **l**eading-**e**dge (ALE) and **a**erodynamic **t**railing-**e**dge (ATE) of the airfoil. The flow responded to the plasma actuation at the ALE by generating organized coherent structures in the shear layer over the separated region. Moderate excitation around the natural shedding Strouhal number

had the most significant effects: synchronizing the shedding from the ALE and ATE, creating moderately sized structures that convected far downstream, greatly reducing the separation area, increasing lift, and decreasing drag. Excitation at much higher Strouhal numbers resulted in the flow returning to its natural shedding state, but with less coherent structures that diffused in the wake. This reduced the separation area and significantly reduced drag. Plasma actuation at the ATE caused a reduction in the magnitude of the fundamental and harmonic peaks in pressure spectra over a broad range of excitation Strouhal numbers. Excitation at the ATE altered the structures over the separated region, suggesting an upstream communication. At excitation frequencies higher than the natural shedding frequency, the natural shedding process was disrupted, weakening the naturally shed structures in the wake. Synchronous excitation at the ALE and ATE was predominantly characterized by the associated ALE excitation. Two cases were found where ATE excitation in addition to ALE excitation had a significant effect, but in those two cases, the flow shared characteristics of individual excitation at the ALE and ATE. The resultant flow was somewhere between the two independent excitations. With asynchronous excitation, the addition of ATE excitation counteracted the lift benefits of ALE excitation. As the ATE excitation increased, the amount of lift decreased. The effect on drag was minimal, suggesting that ALE excitation has a much more significant influence on drag than ATE excitation, even at high ATE frequencies.

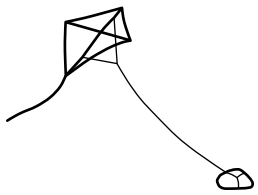

Acknowledgments

I want to thank Dr. Mo Samimy for the opportunity to research under his guidance on many subjects with access to unparalleled facilities. I would like to acknowledge Dr. Igor Adamovich and his laboratory for development of the nanosecond pulse generator. Thanks to Cameron DuBois and Achal Singhal who helped gather and analyze some of the results presented herein. A special thanks to Dr. Nathan Webb and Michael Crawley for all of the helpful discussion and collaborative learning we have shared.

Special recognition is reserved for my wife, Rebecca, for her continual encouragement and support. If I am your rock, then you are my kite, together on the winds of life.

This work is supported by a cooperative agreement with the Army Research Laboratory with Dr. Bryan Glaz and Army Research Office with Dr. Matthew Munson.

Vita

March 22, 1988	Born – Columbus, Ohio
2009–2010	Undergraduate Research Assistant Department of Mechanical Engineering The Ohio State University
2010	B.S. Mechanical Engineering Minor in Mathematics The Ohio State University
2011–present	Graduate Research Associate Department of Mechanical and Aerospace Engineering The Ohio State University

Publications

Archival Publications

C. Clifford, A. Singhal, and M. Samimy. Flow control over an airfoil in fully-reversed condition using plasma actuators. *AIAA Journal*, published online, 2015. doi:10.2514/1.J054157

N. Webb, **C. Clifford**, and M. Samimy. Control of oblique shock wave/boundary layer interactions using plasma actuators. *Experiments in Fluids*, 54(1545), 2013. doi:10.1007/s00348-013-1545-z

C. Clifford. *Design and characterization of a supersonic wind tunnel for the study of shock wave boundary layer interactions.* Mechanical Engineering, Ohio State University, Columbus, 2010.

Conference Publications

C. Clifford and M. Samimy. Flow control on an airfoil in fully-reversed condition with actuation on both leading and trailing edges. In *53rd AIAA Aerospace Sciences Meeting*, number 2015-1266, 2015. doi:10.2514/6.2015-1266

C. Clifford, A. Singhal, and M. Samimy. Leading edge separation control on an airfoil in fully-reversed condition. In *32nd AIAA Applied Aerodynamics Conference*, number 2014-2144, 2014. doi:10.2514/6.2014-2144

C. Clifford, A. Singhal, and M. Samimy. A study of physics and control of a flow over an airfoil in fully-reversed condition. In *52nd AIAA Aerospace Sciences Meeting*, number 2014-1256, 2014. doi:10.2514/6.2014-1265

N. Webb, **C. Clifford**, and M. Samimy. An investigation of the control mechanism of plasma actuators in a shock wave-boundary layer interaction. In *51st AIAA Aerospace Sciences Meeting*, number 2013-0402, 2013. doi:10.2514/6.2013-402

N. Webb, **C. Clifford**, and M. Samimy. Control of oblique shock wave-boundary layer interactions using plasma actuators. In *6th AIAA Flow Control Conference*, number 2012-2810, 2012. doi:10.2514/6.2012-2810

N. Webb, **C. Clifford**, and M. Samimy. Preliminary results on shock wave/ boundary layer interaction control using localized arc filament plasma actuators. In *41st AIAA Fluid Dynamics Conference and Exhibit*, number 2011-3426, 2011. doi:10.2514/6.2011-3426

Fields of Study

Major Field: Mechanical Engineering

Studies in: Subsonic External Flows, Supersonic Internal Flows, Experimental Techniques, Flow Control, Fluid Mechanics, Optical Diagnostics, Turbulence, High-voltage Electronics

Contents

List of Tables

Table **Page**

List of Figures

Figure **Page**

Nomenclature

Roman Letters

A_{sep}	separation area	—
C_D	drag coefficient, see equation 3.3 on page 24	—
C_L	sectional lift coefficient, see equation 3.2 on page 24	—
C_M	pitching moment coefficient, see equation 3.4 on page 24	—
C_p	pressure coefficient	—
c	chord length	mm
c'	blockage height	mm
D	equivalent diameter	mm
f	frequency	Hz
l/d	lift-to-drag ratio, C_L/C_D	—
p, q	pressure	Pa
Re	Reynolds number based on chord, $u_\infty c/\nu$	—
St	Strouhal number, fc'/u_∞	—
U	velocity vector, (u, v)	$\mathrm{m\,s^{-1}}$
U^*	non-dimensional velocity vector, U/u_∞	—
x, y	coordinates	mm

Greek Letters

α	angle of attack	deg.
λ_{ci}	swirling strength	Hz
λ_{ci}^*	non-dimensional swirling strength, $\lambda_{ci}c'/u_\infty$	—
ν	kinematic viscosity of air	$\mathrm{m^2\,s^{-1}}$
ρ	density of air	$\mathrm{kg\,m^{-3}}$
ϕ	phase angle relative to plasma formation	deg.
ω	vorticity, $\nabla \times U$	Hz
ω^*	non-dimensional vorticity, $\nabla^* \times U^*$	—
ξ	dummy variable	*

Subscripts

amb	ambient	—
BL	baseline	—
F	forcing or excitation	—
o	stagnation	—
∞	freestream	—

Acronyms

AC	alternating current	—
ALE	aerodynamic leading-edge	—
ATE	aerodynamic trailing-edge	—
DBD	dielectric barrier discharge	—
NS	nanosecond	—
PIV	particle image velocimetry	—
PSD	power spectral density	—
SOFV	surface oil flow visualization	—
SPL	sound pressure level	—
TKE	turbulent kinetic energy	—

Chapter 1: Introduction

Rotorcraft have a unique place in the aeronautics enterprise. Their vertical take-off and landing, and hover capabilities allow them unprecedented access to locations physically inaccessible to fixed-wing aircraft. The most familiar rotorcraft is the helicopter, widely used in both civil and military applications. However, helicopters have a fundamentally limited forward-flight speed. A traditional helicopter typically utilizes a large rotor atop the aircraft that is solely responsible for both lift and thrust. The rotor faces two major issues during forward flight: compressibility effects and dynamic blade stall. Forward flight increases the rotor's relative speed on the advancing blade side and decreases it on the retreating blade side. On the advancing blade side, the maximum rotor tip speed is typically constrained to avoid tip losses due to compressibility effects [1]. On the retreating blade side, a more aggressive angle of attack is required to balance lift and prevent roll, which could lead to retreating blade stall [2]. The combination of these two effects limits the maximum achievable forward-flight speed.

Time-sensitive missions, such as search and rescue operations, necessitate the development of rotorcraft with greater forward-flight speeds. Slowed-rotor compound vehicles are an emerging class of rotorcraft which achieve that goal by incorporating

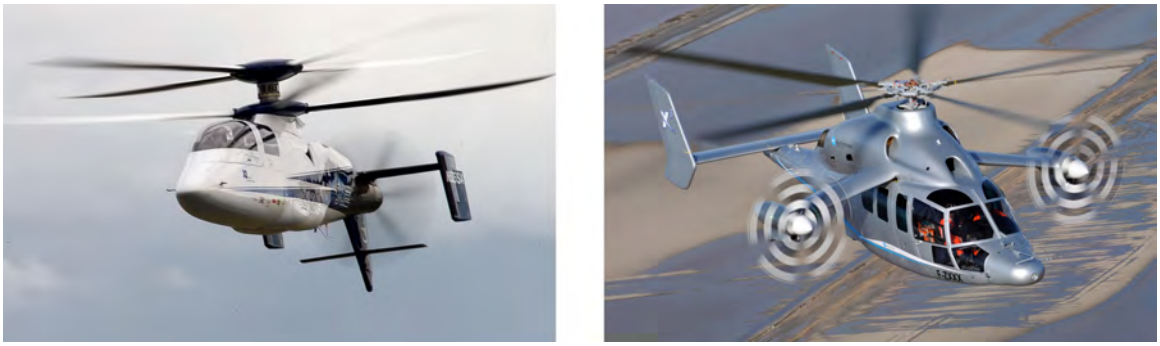

Figure 1.1: Examples of a slowed-rotor compound vehicle: the Sikorsky X2 [8] (left) and the Eurocopter X^3 [9] (right).

aspects of fixed-wing aircraft. Two examples of such compound vehicles are the Sikorsky X2 [3] and the Eurocopter X^3 [4, 5], shown in Fig. 1.1. Slowed-rotor compound vehicles overcome the forward flight limitation by adding an auxiliary form of propulsion, such as a pusher fan, and short wings for increased lift [6]. The addition of a pusher fan, for example, relieves the main rotor of some or all thrust responsibilities and similarly the wing area provides supplemental lift during cruise. Since the main rotor is no longer the sole source of lift and thrust, it may spin more slowly during cruise, allowing for increased maximum forward velocity of the vehicle. However, the simultaneous increase in forward speed and decrease in rotor speed introduces a new issue: a significant portion of the retreating blade side becomes immersed in reverse flow creating a wake and a large drag penalty is incurred [7].

The present work seeks to understand the relevant flow physics and to explore flow control of a NACA 0015 airfoil in fully-reversed condition. Flow control is achieved by using **n**ano**s**econd **d**ielectric **b**arrier **d**ischarge (NS-DBD) plasma actuators. These actuators are surface mounted devices composed of two electrodes separated by a dielectric barrier. The actuators utilize an input signal of periodic pulses that are

of high-voltage and short duration, resulting in rapid plasma formation. Unlike the more widely-studied **a**lternating **c**urrent DBD actuators (AC-DBDs), NS-DBDs exert a negligible body force on the flow [10]. Instead, rapid heating results in thermal and subsequent pressure perturbations that are capable of exciting flow instabilities [10], in a manner similar to that of another class of plasma actuators called localized arc filament plasma actuators [11]. NS-DBDs have been proven as an effective control technique for leading-edge blade stall even at high speeds (typical aircraft take-off and landing speed) [12].

Chapter 2: Background

2.1 Motivation

Slowed-rotor technology allows for an increase in flight speed and cruise efficiency while maintaining the advantages inherent to rotorcraft. Efficiency can be increased by optimizing rotor speed, even at low flight velocities. Such technology has been used in applications like the Bell/Boeing V-22 Osprey, Boeing A-160T, Eurocopter X^3, and the Sikorsky X2 Technology Demonstrator, each of which reduce rotor speed by 10–20% to increase cruise efficiency [6]. The slowed-rotor system used in the X2 allowed it to reach 250 knots in a straight-and-level test flight, making it unofficially the fastest helicopter ever produced [13]. However, the simultaneous increase in forward velocity and decrease in rotor speed introduces new aerodynamic problems. At maximum forward velocity, the advancing rotor tip speed is near Mach 0.85. Due to the trade-off between forward velocity and rotor speed, the flow profile of the retreating blade side changes drastically, as shown in Fig. 2.1. Green indicates flow in the positive direction and red indicates flow in the negative or reverse direction. As the ratio between forward velocity and rotor speed (called the "advance ratio") increases, the velocity at the retreating blade tip decreases and can even be negative at advance ratios greater than one. Thus, at high advance ratios, a significant portion of the

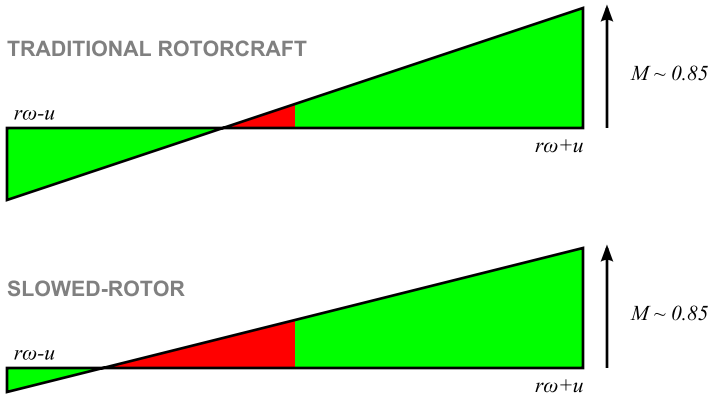

Figure 2.1: Rotor-relative velocity comparison between traditional and slowed-rotor helicopters at top speed.

retreating blade side becomes immersed in reverse flow. Slowed-rotor craft like the Sikorsky X2 result in immersion of as much as 80% of the retreating blade side in reversed flow [6]. Rotor blades of traditional rotorcraft have aerodynamic profiles intended to maximize lift and minimize drag for a particular flow direction. Reversing the flow over such an airfoil results in an aerodynamic bluff body, which creates a wake and incurs a large drag penalty [7].

Flow separation occurs when flow near a wall experiences an adverse pressure gradient that it cannot negotiate. The adverse pressure gradient, when combined with viscous effects of the boundary layer, can reduce the flow momentum enough that a region of zero or negative flow occurs, causing the remaining flow to separate. Flow separation results in a loss of lift and an increase in drag, caused by pressure drag in the wake. On a traditionally oriented airfoil, flow separation decreases suction and leads to a rapid decrease in lift called stall. The separated region, and its associated recirculation, leads to a lower pressure at the trailing-edge resulting in a net increase

in drag. The focus of this work is to reduce flow separation in order to reduce the associated drag penalty.

The defining features of a slowed-rotor compound vehicle are the auxiliary lift and propulsion, rather than the main rotor. As such, there are different design approaches to the main rotor itself. The Eurocopter X^3, like a traditional rotorcraft, utilizes an aggressive angle of attack on the retreating blade side to balance lift and prevent roll. The Sikorsky X2 utilizes coaxial rotors, where a stacked pair of rotors rotate in opposite directions. Due to the counter-rotating nature, both rotors may be offloaded ($\alpha = 0°$) on their respective retreating blade sides while maintaining a balanced lift [14]. Thus, it is of interest to investigate fully-reversed flow on an airfoil with an aggressive angle of attack and with no angle of attack.

The Reynolds number experienced by a rotor blade will vary significantly depending on where the rotor is in its rotation and the forward velocity of the craft. For the simplified case considered here, the Reynolds regime of interest is on the retreating blade side while the craft is operating in forward cruise. Prior research at the Gas Dynamics and Turbulence Laboratory explored the baseline of a NACA 0015 at several angles in reverse flow at Reynolds numbers from $0.25 \cdot 10^6$ to $0.65 \cdot 10^6$ [15]. The Reynolds number based on chord was held fixed at $5.0 \cdot 10^5$ for the research presented herein.

2.2 Bluff Body Flows

Little research has been performed on airfoils in reverse flow, since it is such an unusual configuration. Therefore, an understanding of the flow dynamics must be approximated using simplified geometries. A significant body of research exists

regarding flow over bluff bodies across a range of Reynolds numbers [16, 17]. The flow dynamics behind a bluff body are extremely complex, resulting from an interaction between the boundary layer, the separating free shear layer, and the wake.

At zero angle of attack, the blunt trailing-edge of the airfoil in reverse flow resembles a circular cylinder. The Reynolds-number-dependent instabilities and flow regimes for a circular cylinder occur in the following order: wake transition, shear layer transition, and boundary layer transition [18]. The exact transition Reynolds numbers are very sensitive to surface roughness and freestream turbulence [19]. The Reynolds number considered in this research falls between 10^5 and 10^6, which includes the critical transition regime and part of the supercritical regime. A rapid change in drag and shedding Strouhal number occurs within this range, as shown in Fig. 2.2. The critical transition regime is associated with a reduction of both base suction (surface pressure 180° from the forward stagnation point) and drag due to the formation of a separation bubble on one side of the cylinder. Reattachment of the boundary layer after the separation bubble pushes the final separation as far downstream as 140° from the forward stagnation point. As the separation moves downstream, the width of the wake decreases. In the supercritical regime, two separation bubbles form symmetrically on either side of the cylinder. From Fig. 2.2, the shedding Strouhal number is high relative to the other flow regimes, with typical values of $St \sim 0.4$. The wake is very thin in the supercritical regime and the thickness scales approximately with inverse frequency.

An inclined flat plate serves as a reasonable approximation of an airfoil at nonzero angle of attack. For low Reynolds numbers, the flow over an inclined flat plate will remain laminar and steady; the Reynolds number at which the flow transitions to

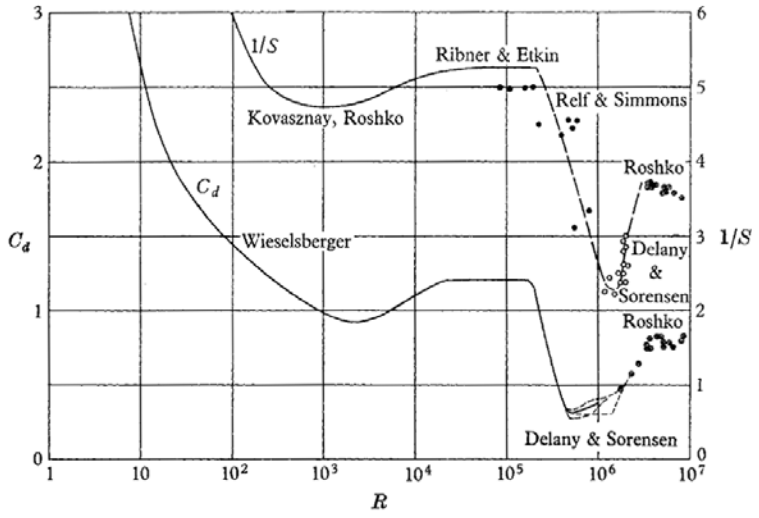

Figure 2.2: Reynolds number dependence of drag coefficient and reciprocal of shedding Strouhal number [19].

a periodic behavior will depend on the angle of attack [20]. Breuer and Jovičić [21] showed similarities in the flow field of a flat plate and a NACA 4415 airfoil at $Re = 2.0 \cdot 10^4$ and $\alpha = 18°$. The flow over the flat plate separated at the sharp leading-edge, forming a shear layer that rapidly transitioned to turbulence. A second, stronger shear layer formed at the trailing-edge; vortices generated at the trailing-edge were found to dominate the flow field [21]. The trailing-edge vortex was attached to the flat plate, growing steadily until it became too large and was shed downstream. A large recirculation region on the suction side of the plate experienced a breathing motion dictated by the trailing-edge vortex. As the vortex increased in size, the recirculating region shrunk. When the vortex was shed, the recirculating region grew into the newly void space until the next vortex began to grow. The result was an asymmetric von Kármán vortex street with vortices of unequal strength. Similar behavior was seen for the NACA 4415 airfoil at the same flow conditions.

Breuer and Jovičić [21] found that the shedding Strouhal number for the trailing-edge vortex based on chord length was $St = 0.636$ for the airfoil and $St = 0.660$ for the plate. A modified Strouhal number was defined, $St' = fc'/u_\infty$, where c' was the blockage height of the plate. At the same Re and α, the modified Strouhal number was $St' = 0.197$ for the airfoil and $St' = 0.204$ for the plate. The modified Strouhal number remained almost constant at $St' \sim 0.15$ for $20° < \alpha < 90°$ and rapidly increased for $\alpha \leq 20°$. Chen and Fang [22] found a similar modified Strouhal number, $St^* \sim 0.16$, for Reynolds numbers between $3.50 \cdot 10^3$ and $32.0 \cdot 10^3$ using an inclined flat plate with beveled edges for $10° < \alpha < 90°$.

Lind *et al.* [23, 24] investigated flow passing an airfoil at static angles in a full 360° arc with Reynolds numbers from $55.0 \cdot 10^3$ to $0.165 \cdot 10^6$. Using smoke flow visualization at $Re = 1.10 \cdot 10^5$ (shown in Fig. 2.3), three unsteady flow regimes were observed on a NACA 0012 in reverse flow. At low angles of attack, the flow remained attached until the curvature at the blunt trailing-edge induced separation, forming a von Kármán vortex street in the wake. Near $\alpha_{rev} = -6°$, the flow was observed to oscillate aperiodically between fully separated and partially reattached. No vortex street was observed, but rather a single shear layer originating from the sharp leading-edge [23]. At higher angles of attack, periodic vortex shedding at the blunt trailing-edge generated structures that were larger and at a significantly lower frequency than in the first regime. The natural shedding Strouhal number (based on projected blockage height) is shown in Fig. 2.4 for a NACA 0012 in reverse flow at $Re = 1.10 \cdot 10^5$. At angles leading up to $\alpha_{rev} = -18°$, the Strouhal number increased rapidly. Beyond this angle, the natural shedding converged to a Strouhal number near 0.16. The authors attribute the variation in Strouhal number to the

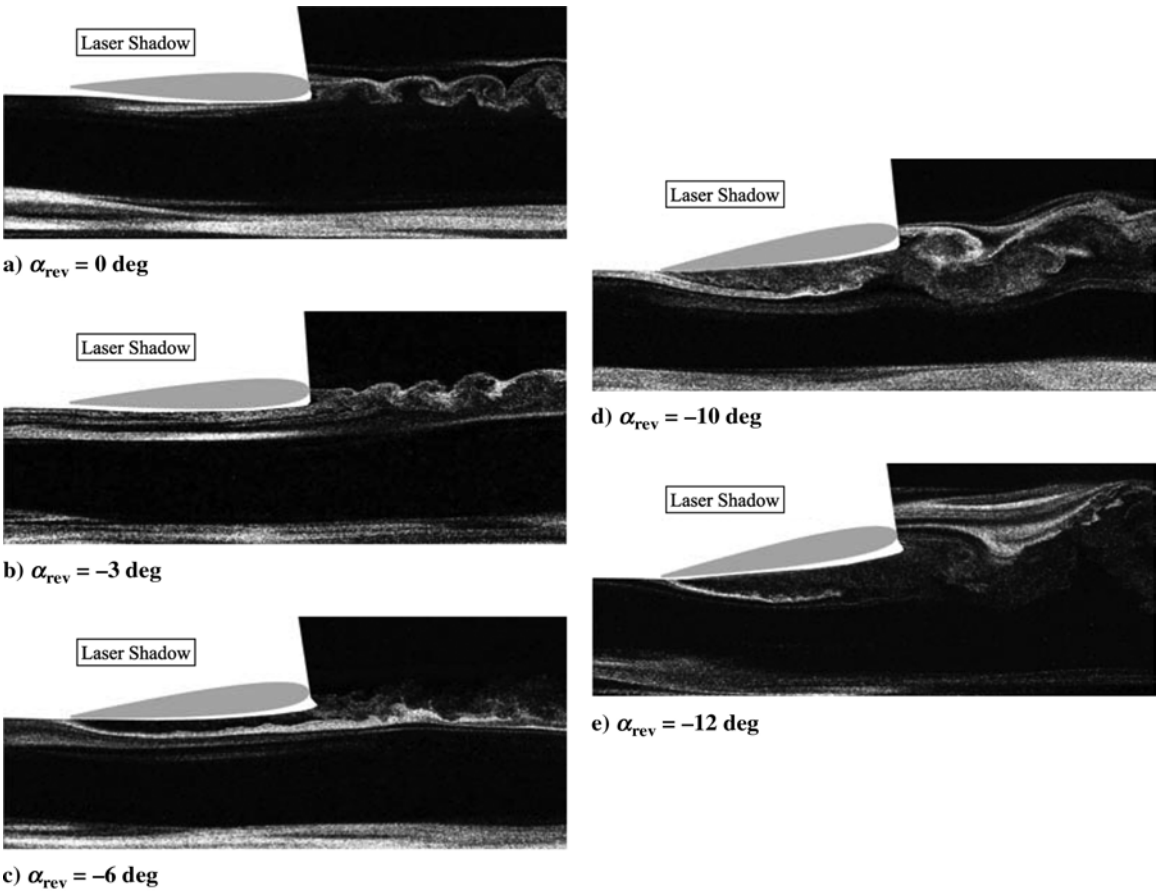

Figure 2.3: Smoke flow visualization of a NACA 0012 airfoil in reverse flow at $Re = 1.10 \cdot 10^5$. Adapted from Lind *et al.* [23].

curvature at the blunt trailing-edge of the airfoil and its effect on flow separation angle [24].

2.3 Aerodynamic Flow Control

Bluff body flows, such as those described above, produce significant unsteadiness resulting in lift fluctuations, vibration, noise due to vortex shedding, and increased drag [25]. Substantial development of flow control techniques applied to such flows

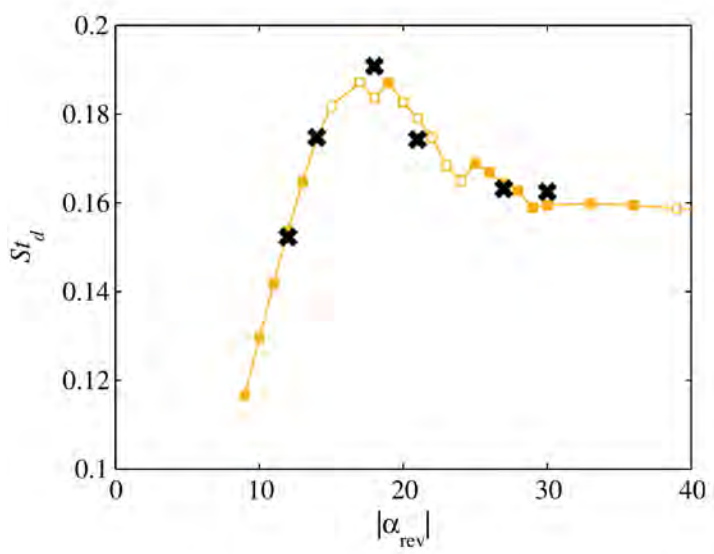

Figure 2.4: Vortex shedding Strouhal number of a NACA 0012 in reverse flow at $Re = 1.10 \cdot 10^5$ [24].

has been done [26]. These techniques either enhance or attenuate natural flow instabilities to produce the desired effect. Flow control methods are broadly categorized into either active or passive control. Passive methods modify the flow via geometric modifications such as increased surface roughness (often called a "trip strip" and used to expedite transition to turbulence) or surface mounted vortex generators. Although these modifications are effective under design conditions, they are often inefficient or even detrimental at off-design conditions. Active flow control is an alternative to passive, using techniques such as piezoelectric oscillation, blowing/suction, and plasma formation. Active excitation at frequencies near that of a natural flow instability triggers the subsequent growth of instability waves. Active methods may be either open-loop, which operate in a predefined manner, or closed-loop, which operate according to feedback gathered by sensors in the flow.

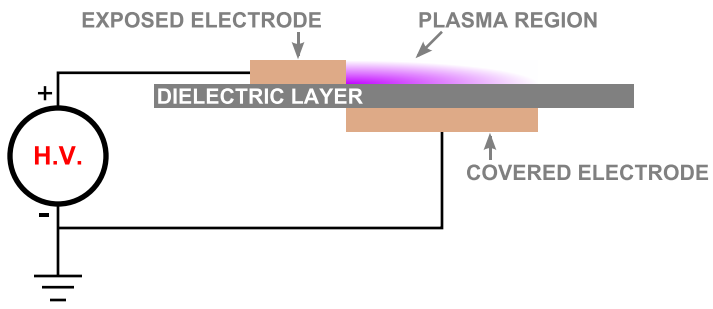

Figure 2.5: Schematic of a DBD. Two electrodes are separated by a dielectric barrier and driven by either an AC or NS input signal, causing plasma to form over the covered electrode.

Plasma actuators are attractive as a flow control system because they are surface mounted, lack mechanical parts, are small and lightweight, and have low power requirements. Unlike many zero-net-mass flux devices, which are driven by an electromechanical driver with limited bandwidth and are prone to mechanical failure, plasma actuation is capable of providing high-bandwidth excitation without moving parts [12]. The DBD plasma actuator has gained in popularity recently due to its simple construction and ease of implementation. These actuators are surface mounted devices composed of two electrodes separated by a dielectric barrier, as illustrated in Fig. 2.5. High-voltage, short-duration pulses are applied to the exposed electrode which, combined with the grounded covered electrode, creates a strong electric field resulting in rapid plasma formation. Currently, there are two types of signals used to drive the DBDs: high-voltage AC and NS-pulse inputs.

AC-DBD plasma actuators have been extensively studied and achieve control authority through momentum addition [27]. The control mechanism for AC-DBDs is electrohydrodynamic in nature and results from charged species colliding with neutral

species causing a direct momentum addition near the wall. The induced near-wall jet can reach 10 m/s in quiescent air for a typical actuator geometry and AC input signal [28]. AC-DBDs lack sufficient control authority at high Mach numbers where it is difficult to produce sufficient momentum for control.

NS-DBD plasma actuators are a recent development of DBD actuators. They are physically identical to AC-DBDs, but utilize repetitive high-voltage (5–20 kV) pulses of short duration (tens to hundreds of nanoseconds) [28]. Unlike AC-DBDs, NS-DBDs exert a negligible body force on the flow. Instead, rapid heating results in thermal and subsequent pressure perturbations that generate nominally two-dimensional cylindrical and planar compression waves [10]. A series of spherical waves form along the span of the actuator, which sum to form a cylindrical compression wavefront. The thermoacoustic waves are capable of perturbing natural flow instabilities to achieve control authority even at very high Reynolds and Mach numbers [12, 29, 30].

Previous work has been done using NS-DBDs for leading-edge control on a conventionally oriented airfoil in deep stall [10, 12, 30, 31]. It was found that NS-DBDs excite natural flow instabilities, causing the generation of large coherent spanwise vortices, which entrain high-momentum fluid into the separated region, thus improving lift and reducing drag [10, 12]. Although the leading-edge is not sharp in the conventional orientation, deep stall behavior is essentially that of a bluff body. Thus, it is expected that similar control authority will be demonstrated at angle of attack.

A literature review yielded no examples of NS-DBDs being used successfully on the wake of a circular cylinder. However, effective wake control has been achieved using AC-DBD plasma actuators [32–34]. NS-DBDs have been used to manipulate the bow shock of a circular cylinder in supersonic flow [30], demonstrating the potential

of NS-DBD actuators even at high Mach numbers. Wake control schemes found in the literature often modify the recirculation region directly, which in turn modifies the wake. For example, the use of an end plate [35, 36], splitter plate [16, 37, 38], or secondary cylinder [39, 40] prevents the unsteady motion of the separated region, thus preventing the formation of a von Kármán vortex street. The use of base bleeding [41, 42] or active blowing/suction [43] alters the size of the recirculation, thus altering the aerodynamic characteristics. At this point, it is unclear whether NS-DBD excitation will be effective at zero degrees.

Chapter 3: Experimental Methods

3.1 Experimental Facility

Experiments were performed in the recirculating wind tunnel located at the Gas Dynamics and Turbulence Laboratory, within the Aerospace Research Center at The Ohio State University [10, 12]. The tunnel has an optically-clear acrylic test section with internal dimensions measuring 0.61×0.61 m in cross-section and 1.22 m in length. Two acrylic disks, 305 mm in diameter, are positioned in the center of each sidewall. An airfoil is mounted between the disks, which are able to rotate continuously, allowing for any angle of attack setting. However, the edges of each disk obstruct visual access, corrupting optical diagnostics (such as PIV) in a circular arc. A photo of the test section with airfoil installed is shown in Fig. 3.1. The test section ceiling is slotted along the centerline to allow for instrumentation access. A two-axis traverse mounted atop the test section allows for precise positioning of instrumentation, such as a hot-wire or microphone. The slot is sealed with a high-density nylon brush.

Flow is generated by an axial fan powered by a three-phase induction motor with variable frequency drive capable of running from 0 to 60 Hz in 0.1 Hz increments. Turning cascades are used to minimize losses and the flow is conditioned using a hexagonal-cell honeycomb upstream of the converging section. The tunnel is capable

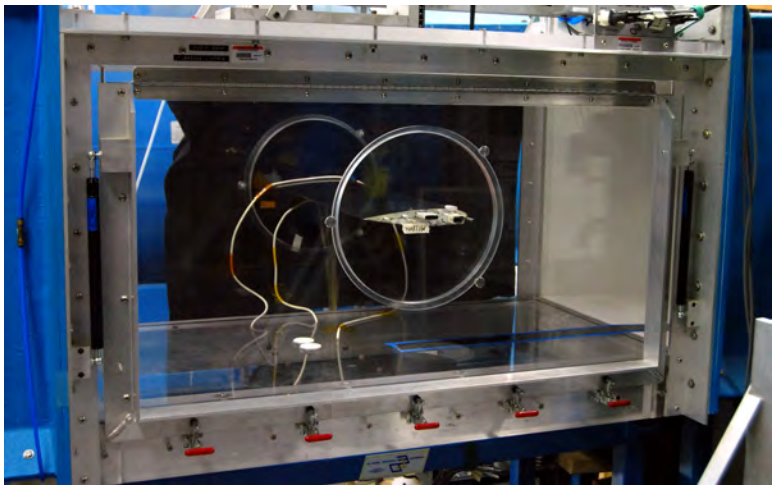

Figure 3.1: Test section of low-speed recirculating wind tunnel at OSU ARC.

of producing a continuous range of flow velocities of 3–95 m/s, although velocities below 10 m/s suffer from significant flow unsteadiness [44]. The corresponding Reynolds numbers based on chord length, $Re = u_\infty c/\nu$, are $4.0 \cdot 10^4$–$1.2 \cdot 10^6$ for a chord length of 203 mm. Freestream turbulence is less than 0.25% at fan speeds below 40 Hz, corresponding to a Reynolds number near $7.8 \cdot 10^5$, and less than 1% at higher speeds.

Freestream static and stagnation pressure (p_∞ and p_o) are measured using two piezometer rings, consisting of four pressure taps each, at either end of the converging section connected to Omega Engineering pressure transducers (models PX655-25DI and PX655-5DI). A thermocouple located downstream of the test section, before the turning vanes, is used to monitor freestream temperature T_∞. Ambient temperature T_{amb} is measured using the same thermocouple, prior to tunnel startup. Ambient pressure p_{amb} is collected from METARs data reported by the OSU Airport (KOSU). Freestream velocity is calculated using Bernoulli's Equation:

$$u_\infty = \sqrt{2k\left(\frac{p_o - p_\infty}{\rho}\right)} \tag{3.1}$$

with a corrective factor of $k = 1.05$, which was empirically determined using a calibrated hot-wire anemometer [44].

A NACA 0015 airfoil was used for this initial study, even though it is not typically used in rotorcraft, in order to simplify the problem. Prior work explored the baseline case of the same airfoil at several angles in reverse flow at Reynolds numbers from $0.25 \cdot 10^6$ to $0.65 \cdot 10^6$ [15]. The airfoil has a 203 mm chord and spans the test section. Thirty-five static pressure taps, 0.7 mm in diameter, are distributed around the airfoil near the centerline. The concentration of taps is greatest at the geometric leading-edge, where the suction peak would typically be located. Seven Kulite pressure transducers (models XCQ-080-25A, XCQ-080-5D, and LQ-062-25A) are flush mounted along one side of the airfoil; however, they were not utilized in this study. The transducers are sufficiently far from plasma formation to avoid any arcing between the actuators and the metal transducers.

The angle of attack is set by rotating the acrylic disks on either side of the airfoil, which are secured by tightening several thumb screws. The angle is measured using a digital angle meter on one of the airfoil spars. The same surface of the same spar is always used, resulting in a repeatability of $\pm 0.1^\circ$. The angles of attack considered were 0° and 15°, both at a Reynolds number of $5.0 \cdot 10^5$.

Two coordinate systems are used throughout this thesis. Both coordinate systems have their origin at the **a**erodynamic **t**railing-**e**dge (ATE), as shown in Fig. 3.3. The opposite edge is referred to as the **a**erodynamic **l**eading-**e**dge (ALE). The first system is a straight line along the chord line normalized by the chord length, denoted x/c, where positive coordinates indicate the aerodynamic suction side and negative coordinates indicate the aerodynamic pressure side. This system is in the airfoil reference

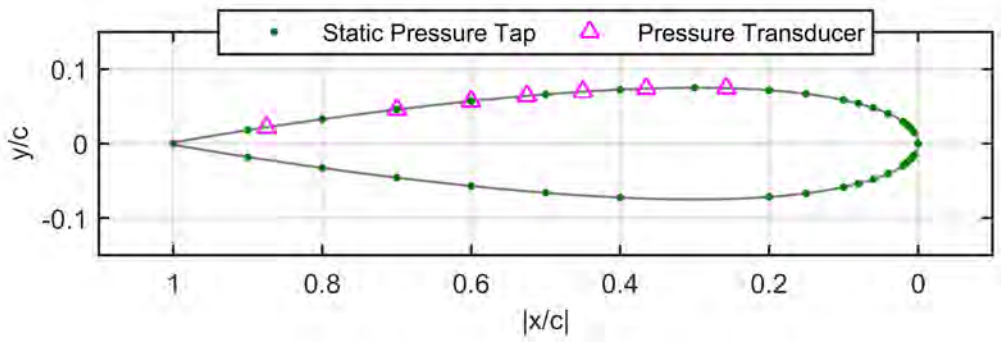

Figure 3.2: Airfoil profile and onboard instrumentation.

frame and is used to indicate on-board instrumentation, actuators, and the flow separation line. The second system is a two-dimensional grid aligned with the test section and normalized by airfoil thickness, denoted x/D and y/D. The variable D was chosen since the flow behind the airfoil at $\alpha = 0°$ is similar to the wake of a bluff-body of diameter D. This system is in the test section reference frame and is used to indicate other instrumentation, such as microphone locations (indicated in Fig. 3.3) and velocity data.

3.2 Actuator Construction and Characterization

Four actuators were placed symmetrically on the airfoil: one on the top surface and one on the bottom surface at both ALE and ATE. Each actuator was constructed of two 0.09 mm thick copper tape electrodes; the exposed high-voltage electrode was 6.35 mm wide and the covered ground electrode was 12.7 mm wide. The total length of each electrode was approximately 560 mm. The dielectric layer was composed of three layers of Kapton tape, each 0.09 mm thick with a dielectric strength of 10 kV.

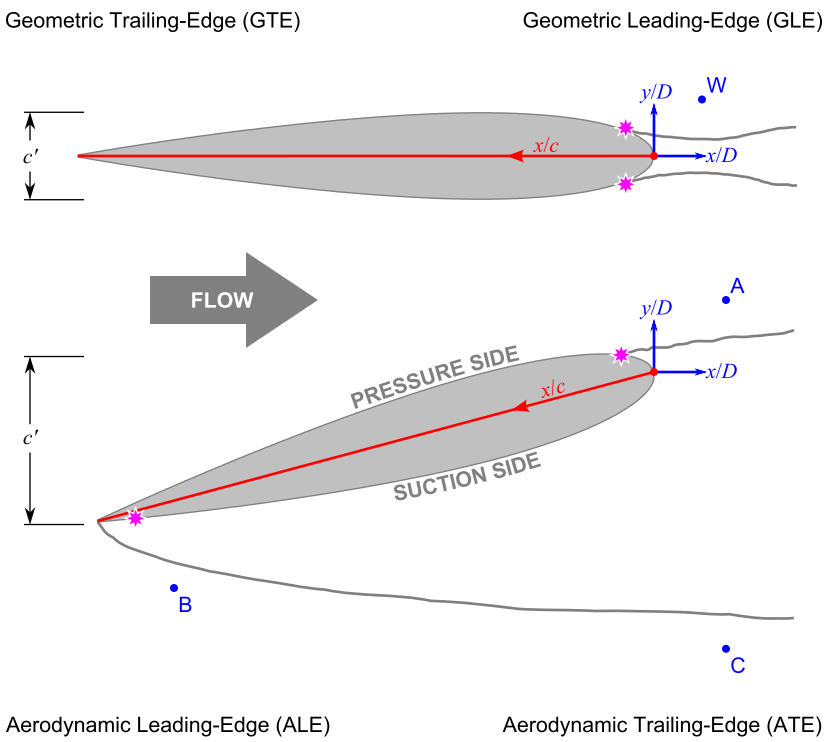

Figure 3.3: Schematic of experimental arrangement.

The total thickness of each actuator was a mere 0.45 mm. Actuators were constructed by hand with an estimated error of less than 2 mm.

Placement of the actuators was determined by **s**urface **o**il **f**low **v**isualization (SOFV) and geometric constraints. The ATE actuator junctions were located at $x/c = \pm 0.070$, as indicated by the right half of Fig. 3.4, with the plasma formation regions extending to $x/c = \pm 0.133$. ATE placement was chosen based on SOFV which showed flow separation at $x/c = \pm 0.055$ at $\alpha = 0°$. The ALE electrode junctions were located at $x/c = \pm 0.945$, as indicated by the left half of Fig. 3.4, with the plasma formation regions extending to $x/c = \pm 1.00$. There was a slight overlap between the two covered electrodes at the ALE where the edge of the electrodes meet at the sharp end of the

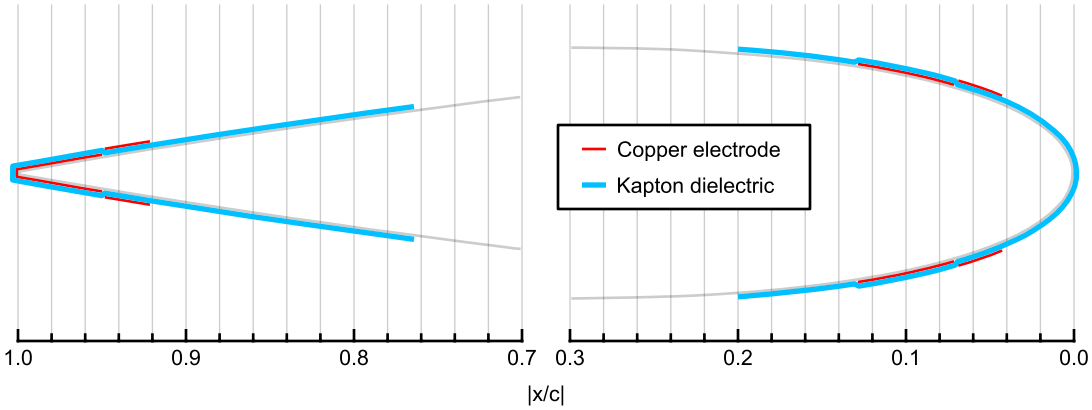

Figure 3.4: Actuator placement on each end of the NACA 0015. Actuator thickness is exaggerated.

airfoil. This placement was chosen, as it was the furthest upstream position possible without changing the electrode geometry (*i.e.* using a narrower covered electrode). The symmetric installation of actuators allowed for instrumentation on either side of the wake by inverting the angle of attack.

The NACA 0015 used in this study has an interchangeable geometric leading-edge. One of the interchangable pieces has a recess so that an actuator may be installed flush with the airfoil surface and the other is smooth for a high-quality baseline. The intent of this interchangeable design was to allow direct comparison of the baseline with installed actuator to that of a clean airfoil, confirming that the actuator presence had negligible impact on the flow [44]. In this study, the smooth geometric leading-edge was utilized so that actuators could be freely located. As a consequence, the actuators are surface mounted rather than flush mounted and therefore present a step discontinuity to the flow. However, the dielectric tape extends several centimeters in either direction beyond the actuator, as shown in Fig. 3.4. Thus, in addition to being very thin, the discontinuity at the edge of the tape is far from the sensitive regions

of the developing boundary layer. Furthermore, in the fully-reversed case, the flow is massively separated and the airfoil behaves like a bluff body. The intricacies of the airfoil profile are unlikely to have any significant effect on the flow field for this reason.

The actuators were driven by high-voltage nanosecond pulses generated using one or two pulse generators designed and constructed in-house. The pulse generators, depicted in Fig. 3.5, are located inside of the tunnel loop to minimize wire length to the actuators. Each pulse generator utilizes a magnetic compression circuit capable of repetition rates of up to 2 kHz for one unit and 10 kHz for the other. The limitation on pulse repetition is primarily heat management and the two units differ only in their cooling systems. These repetition rates are based on 60 second run-times and may be elevated if shorter run-times are enforced. Peak voltage on an open load can reach $\sim$18 kV with a maximum pulse energy of $\sim$100 mJ. Pulses can be either positive or negative polarity, but only positive polarity pulses were used in this work. A Sorenson DC power supply (model DCR 600-4.5B) is used to generate a supply voltage of up to 600 V_{DC}, which is then compressed and amplified by the pulse generator. Assuming fixed geometry of the actuator and lead wires, supply voltage directly controls the coupled pulse energy of the actuators. Throughout this work, the supply voltage was held fixed at 450 V_{DC} for single-excitation cases and 470 V_{DC} for simultaneous-excitation cases. The simultaneous-excitation voltage was selected such that each actuator had a coupled pulse energy approximately equal to the single-excitation cases.

Representative discharge characteristics were acquired for a 560 mm long actuator driven at 100 Hz. Voltage and current traces of the actuators were gathered using a

Figure 3.5: Nanosecond pulse generators located inside of the tunnel loop. From left to right: main unit, low-voltage DC power supply, control unit. High-voltage DC power supply not shown.

LeCroy Wavejet oscilloscope (model 324A). A Tektronix high-voltage probe (model P6015A) was situated across the high-voltage terminals of the pulse generator and a Pearson current monitor (model 2877) was placed on the ground side of the circuit, between the actuator and the pulse generator. The voltage and current traces shown in Fig. 3.6(a) were acquired simultaneously and ensemble-averaged over 256 discharge pulses. Energy and power were calculated offline from the recorded voltage and current. The instantaneous power and time-resolved coupled pulse energy are shown in Fig. 3.6(b). The peak voltage and current were approximately 8 kV and 27 A, respectively. A peak power of 180 kW was discharged, but due to the short pulse width, steady state energy consumption was just 3 mJ per pulse. For the frequencies

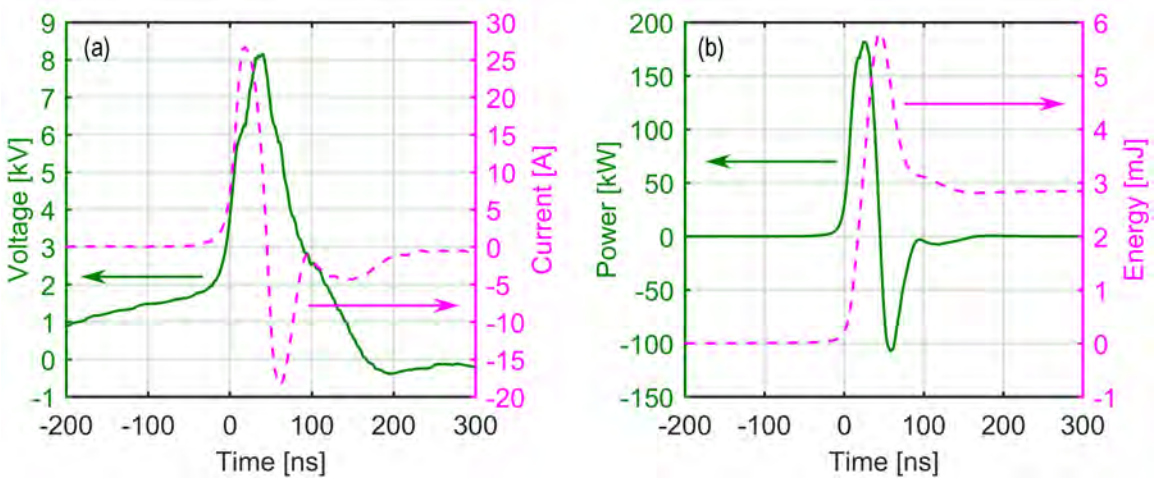

Figure 3.6: Representative traces of (a) voltage and current and (b) instantaneous power and energy for a 560 mm long actuator driven at 100 Hz.

considered here (less than 2 kHz), this corresponds to time-averaged power of less than 6 Watts.

3.3 Surface Oil Flow Visualization

Surface **o**il **f**low **v**isualization (SOFV) utilizes shear stress at the wall to distort a thin application of oil to indicate near-wall flow features. This makes it useful for characterizing regions of separated flow, since the oil in the separated region will be either undisturbed or flowing in the reverse direction. Titanium white oil-based paint was mixed with SAE 85W-140 gear oil at a mass ratio of 1:4. The mixture was spread thinly and evenly by hand in a roughly 50×100 mm rectangular patch at the ATE. Application was performed using one finger with a latex glove which resulted in a finish smoother than possible using a brush, making ripples due to shear more apparent. The mixture was applied off-center to avoid the static pressure taps (discussed in the next section). The wind tunnel was quickly brought to the desired flow velocity and

allowed to run until the mixture had moved enough to clearly indicate separation. Photographs of the mixture were acquired with the tunnel in operation, then the tunnel was abruptly stopped (to minimize disturbance) and more closely examined.

3.4 Static Pressure

Static pressure measurements on the airfoil surface are used to calculate lift, drag, and pitching moment. These metrics provide a macroscopic view of the airfoil performance. In addition, surface static pressure provides insight on the flow behavior in the near-wall region, which is difficult to resolve using PIV (discussed below). Static pressure measurements were acquired using three Scanivalve digital pressure sensor arrays (model DSA3217). The pressure coefficient, $C_p = (p - p_\infty)/q_\infty$, was averaged over 100 samples acquired at 1 Hz near the centerline, where p is the static pressure, p_∞ is the freestream static pressure, and q_∞ is the freestream dynamic pressure. The sectional lift coefficient C_L, drag coefficient C_D, and pitching moment coefficient at quarter-chord C_M, were calculated using the line integrals about the surface of the airfoil as in Eqns. 3.2–3.4 where θ is the surface-normal angle and ds is the arc length.

$$C_L = -\int_{-1}^{1} C_p \sin\theta \, ds \tag{3.2}$$

$$C_D = -\int_{-1}^{1} C_p \cos\theta \, ds \tag{3.3}$$

$$C_M = \int_{-1}^{1} C_p \left(0.25 - |x/c|\right) \sin\theta \, ds - \int_{-1}^{1} C_p \left(y/c\right) \cos\theta \, ds \tag{3.4}$$

These metrics neglect viscous effects and account only for the pressure. However, bluff body flows are defined by the dominance of pressure drag over viscous drag, therefore the contribution of viscous effects is assumed negligible. The 95% confidence interval for C_p measurements is smaller than the presented symbol size in all cases.

However, since the actuators cover some of the static pressure taps and the spatial resolution at the ALE is rather poor, these measurements serve only as an estimate.

3.5 Pressure Spectra

Pressure spectra near the wake was used extensively as a preliminary diagnostic, since it is quick to acquire and process, allowing a large parameter space to be explored in a short amount of time. A Brüel & Kjær (B&K) 1/4-inch microphone (model 4939) and preamplifier (model 2670) were used with a B&K NEXUS signal conditioner (model 2690) to acquire time-accurate pressure data. The microphone circuitry was found to have robust resistance to electromagnetic interference from the actuators. The microphone voltage was bandpass filtered between 20 Hz and 100 kHz (resulting in effectively unfiltered data for the frequencies considered here) and acquired using a National Instruments PCI-6143 analog input board with LabVIEW software. The frequency response of the microphone is flat up to 40 kHz with grid cap installed. For each experimental case, data was collected in 60 blocks of 16,384 samples each at a sampling rate of 10 kHz. The **p**ower **s**pectral **d**ensity (PSD) was calculated for each block, then the collection of PSDs were ensemble-averaged, and finally the average was converted to decibels (dB) using a reference pressure of 20 μPa. Strouhal numbers were calculated using the blockage height of the airfoil, $St = fc'/u_\infty$, as done by Breuer and Jovičić [21] and Lind *et al.* [23, 24]. The blockage height was found by projecting the airfoil profile onto a flow-normal plane. The blockage height was $c' = D = 30.5$ mm at $\alpha = 0°$ and $c' = 59.0$ mm at $\alpha = 15°$.

Probe locations were determined using vorticity maps calculated from PIV data. Each shear layer is highlighted by a region of high vorticity magnitude. The locations

were approximately $0.5D$ from the edge of the nearest shear layer to avoid interaction of the probe with the shear layer. After the locations were determined, they were printed onto a template that could be affixed to the airfoil. The microphone was then manually positioned using a two-axis traverse until it aligned with one of the points with an estimated error of less than 1 mm.

3.6 Particle Image Velocimetry

Two-component **p**article **i**mage **v**elocimetry (PIV) was the primary diagnostic technique. PIV is a quantitative technique that enables the mapping of the velocity and vorticity fields. Ensemble averaging of the instantaneous images provides a view of the time-averaged flow over the airfoil and in its wake. Although this technique is very informative, it is also very time consuming to acquire and process; thus, the diagnostic techniques mentioned above were typically employed first and PIV was reserved only for the most promising cases. PIV data was acquired for both the flow over the suction side of the airfoil and behind the ATE. Maps of normalized velocity magnitude, $|U^*|$, normalized vorticity, $\omega^* = \nabla^* \times U^*$, and **t**urbulent **k**inetic **e**nergy (TKE) are shown to characterize the flow. The streamwise and vertical axes are normalized by the equivalent diameter, $D = 30.5$ mm.

Seed particles were injected into the tunnel upstream of the converging section. Atomization was achieved using either a TSI 6-jet atomizer (model 9306A) with extra virgin olive oil or a LaVision aerosol generator with DEHS fluid. Both atomizers provide nominally submicron seed particles and were equally well-suited to seed the flow. Illumination of the seed particles was provided by a Spectra Physics PIV-400 double-pulsed Nd:YAG laser, with a nominally 10 Hz repetition rate. The beam is

directed over a distance of ∼6 m then formed into a sheet using a 1 m focal length spherical lens and two −25 mm focal length cylindrical lenses. The beam forming optics may be mounted in two possible positions atop the test section, illuminating either the separated region or the wake. The spanwise location of the sheet may be adjusted by sliding the optics along an optical rail and the streamwise position may be fine-tuned by minor adjustments of the first cylindrical lens. Despite being mounted directly to the tunnel, no serious vibrations of the beam forming optics have been encountered. Alignment of each laser pulse is performed using burn paper and fine-tuned by visual inspection of the particle movement between two frames of raw data.

Two camera arrangements were used to acquire PIV data. The preliminary setup, depicted on the left in Fig. 3.7, utilized a LaVision 14-bit 2048×2048 pixel Imager Pro-X camera body with Nikon Nikkor 50 mm f/1.2 lens. The end of the lens was positioned ∼650 mm from the test section wall such that the field of view contained either the separated region or the wake region. In the wake region case, a very small portion of the ATE was visible such that a spatial reference was available. Experiments were performed twice: once with the camera in each position, which necessitated adjustment of the sheet forming optics, calibration of the PIV system, acquisition of the data, ensemble or phase averaging, and then finally stitching the two halves together. This setup was capable of 10 Hz acquisition.

Further experiments were performed using a two camera setup, depicted on the right in Fig. 3.7, which utilized two LaVision 12-bit 2048×2048 px Imager Pro camera bodies each with a Nikon Nikkor 35 mm f/1.2 lens. The cameras were positioned in parallel ∼170 mm center-to-center with each lens ∼540 mm from the test section

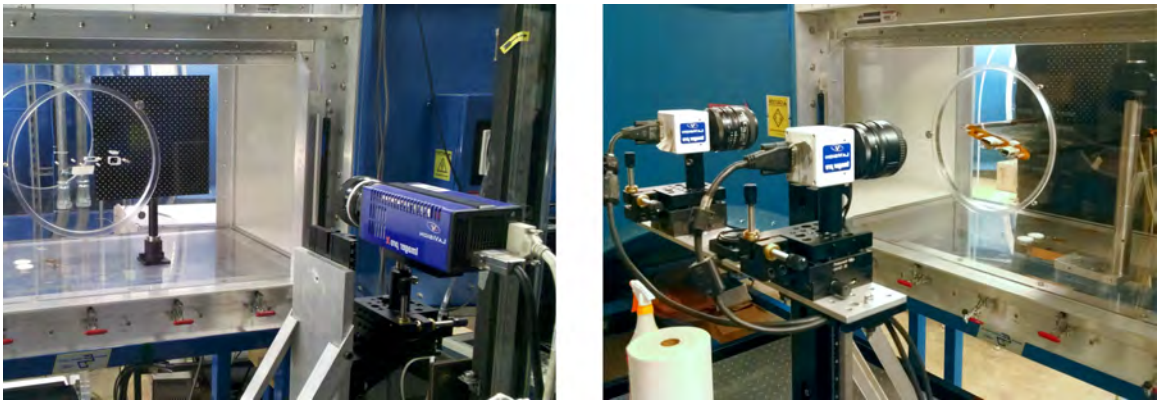

Figure 3.7: Experimental arrangement of the PIV system: one-camera setup (left) and two-camera setup (right).

wall such that there was a slight overlap in the fields of view, but neither camera was obstructed by the acrylic disk. Both cameras were calibrated simultaneously using the "side-to-side" calibration process described by LaVision. The wider field of view was illuminated by moving the two cylindrical lenses farther up the beam path; this necessitated removing the spherical lens which could not be adequately positioned without either cropping the edges of the laser sheet or making a sheet which was too thin. This allowed for acquisition of the entire flow field in a single experiment without visual obstruction of the acrylic disk. Furthermore, since the two cameras acquired data synchronously, an instantaneous view of the entire flow field was made available. This setup was capable of 5 Hz acquisition; despite the slower acquisition rate, simultaneous acquisition made this setup quicker overall.

For each image pair, multipass cross-correlation was performed using a decreasing window size from 32×32 px to 16×16 px with 50% overlap and 75% overlap, respectively. A final pass was performed using high accuracy Whittaker reconstruction (10×10 px). The resulting velocity fields were post-processed to remove spurious

vectors using a correlation peak ratio criteria, allowable vector range, and median filter based on nearest-neighbor. The removed vectors were iteratively replaced where possible, but never interpolated. Prior experience showed that the use of interpolation adversely affected turbulent statistics. Therefore, statistical measures (mean and standard deviation) made use of all available samples for each vector, but the number of samples may be less than the total number of image pairs. A 3×3 px Gaussian smoothing filter was then applied. Finally, the two halves of the flow field were combined. In the two-camera setup, instantaneous vector fields were seamlessly blended using DaVis software before any statistics were calculated. In the one-camera setup, after statistics were calculated, the scalar fields were cut and spliced together at a given streamwise coordinate.

Full scale error of instantaneous velocity and uncertainty of mean quantities are shown in Table 3.1. Full scale error (in m/s) was calculated using

$$\epsilon_{vel} = 10^3 \cdot \frac{\epsilon_{cp}}{S\,dt} \tag{3.5}$$

where ϵ_{cp} is the correlation peak estimation error in px, S is the scale factor in px/mm, dt is the laser pulse separation in μs, and 10^3 accounts for non-SI units. Laser timing error was assumed negligible and ϵ_{cp} was estimated as 0.1 px [45]. Uncertainty of mean quantities were calculated using 95% confidence intervals:

$$\mathrm{CI} = 1.96 \cdot \frac{\xi_{rms}}{\sqrt{n}} \tag{3.6}$$

where ξ_{rms} is the standard deviation of the samples and n is the number of samples. Recall that these calculations are done on an individual vector basis, using the maximum number of samples available for each vector. Values are reported relative to freestream velocity u_∞ in a range, where the minimum uncertainty was in the

Setup	Instantaneous U	Mean $\lvert U^* \rvert$	ω^*	TKE
One-camera	1.0	0.2–3	0.1–2	$\leq$3
Two-camera	1.3	0.1–2	$\leq$1	$\leq$2

Table 3.1: Uncertainty (%) in PIV measurements.

freestream and the peak uncertainty was in the separated or wake region. The time between subsequent laser pulses in the two-camera setup was based upon the convective velocity rather than the freestream velocity; this resulted in a slightly larger full scale error, but reduced uncertainty in the mean quantities due to improved vector correlations.

The excitation effects and mechanism were explored using phase-locked PIV. A heavily EMI-shielded cable between the NS-DBD control and PIV computers provided an always-on synchronization signal based on excitation frequency. Active synchronization, even when the actuators were disabled, ensured laser stability. Instantaneous images were captured similar to standard PIV, but were synchronized with specific phases throughout the excitation period and then ensemble-averaged. The resulting data is referred to as phase-averaged. The reference time (in milliseconds) to achieve a particular phase was calculated using

$$t_{\text{ref}} = \frac{\phi}{360}\frac{1000}{f_{\text{F}}} - t_{\Delta} \tag{3.7}$$

where ϕ is the desired phase and f_{F} is the excitation frequency. The delay between the trigger signal and plasma formation t_{Δ} was subtracted so that plasma formation occurred at 0°. If the resultant t_{ref} was less than 0.4 ms, another full period ($1000/f_{\text{F}}$)

was added to satisfy the minimum reference time in DaVis. Initially, this was calculated by hand for each excitation frequency, but was later incorporated into the synchronization code. The phases considered here were $\phi = 0°$, 90°, 180°, and 270°.

Non-dimensional swirling strength, $\lambda_{ci}^* = (\lambda_{ci} c')/u_\infty$, was used as the vortex identification technique. Unlike vorticity, which identifies both rotation and shear, swirling strength effectively negates shear and highlights only rotation. This is a critical-point method using the local velocity gradient tensor and its eigenvalues, as detailed by Adrian *et al.* [46]. Although only two components of velocity were available (u and v), a three-dimensional tensor was utilized assuming incompressibility in the spanwise direction. The velocity gradient tensor is shown in Eqn. 3.8 where the gradient has been applied to the phase-averaged velocity field $\tilde{U}$. Swirling strength is quantified by the largest imaginary component of the eigenvalues of $\nabla\tilde{U}$. The tensor was calculated using a second-order accurate central difference scheme and the eigenvalues were found using MATLABs built-in `eig()` command.

$$\nabla\tilde{U} = \begin{pmatrix} \partial_x\tilde{u} & \partial_y\tilde{u} & 0 \\ \partial_x\tilde{v} & \partial_y\tilde{v} & 0 \\ 0 & 0 & -\partial_x\tilde{u} - \partial_y\tilde{v} \end{pmatrix} \tag{3.8}$$

An alternate phase-locking method that synchronized with the shedding of vortices, rather than plasma formation, was also employed. The B&K microphone and signal conditioner mentioned above were used in conjunction with in-house software to provide a trigger signal based on vortex shedding events. The software acquires real-time pressure data, applies a first-order Butterworth bandpass filter about the shedding frequency, and outputs a square-wave trigger on a rising edge. This process was performed at 2 kHz, thus the time between pressure input and trigger output was less than 0.5 ms. Bandpass limits were determined *in situ* by gathering a sample

spectrum and finding the left and right shoulders of the natural shedding peak. The voltage threshold to output a square wave had to be set low (near zero) to maintain laser stability, which resulted in spurious triggers. A conditional-average based on covariance was used in post-processing to filter out spurious trigger events. This method allows the naturally shed large-scale structures to be captured when the shedding frequency does not lock to excitation and also allows a phase-locked baseline to be acquired.

Chapter 4: Zero-Degree Angle of Attack

Ensemble-averaged baseline PIV images are shown in Fig. 4.1. The line near $x/D = 1$ is the edge of an acrylic disk used to mount the airfoil. At this angle of attack, the flow behind the airfoil is effectively a bluff-body wake flow. The wake is narrow with a small region of recirculating flow and symmetric regions of high vorticity on either side, similar to that of a flow behind a cylinder [18]. The two regions of vorticity are opposite in sign and decrease in strength as they diffuse downstream.

The separation line was determined using SOFV, as shown in Fig. 4.2. Downstream of the red line, which is located at $|x/c| = 0.055$, the oil/paint mixture is relatively undisturbed indicating separated flow. This measurement was used for the placement of the NS-DBDs, which were located $\sim$3 mm upstream of the separation line. The receptivity of a free shear layer is maximum at the shear layer origin, but it is generally higher when the perturbations are located upstream rather than downstream [47–50]. Since the shear layers of a circular cylinder wander [18], a slightly upstream location was chosen to ensure that perturbations were always upstream.

Pressure spectra were obtained near the wake (point W in Fig. 3.3) to investigate vortex-shedding frequency. The vorticity map shown in Fig. 4.1(b) was used to determine a suitable microphone location. Although the microphone was placed outside of the shear layer, the positioning was close enough that the spectrum was predominately

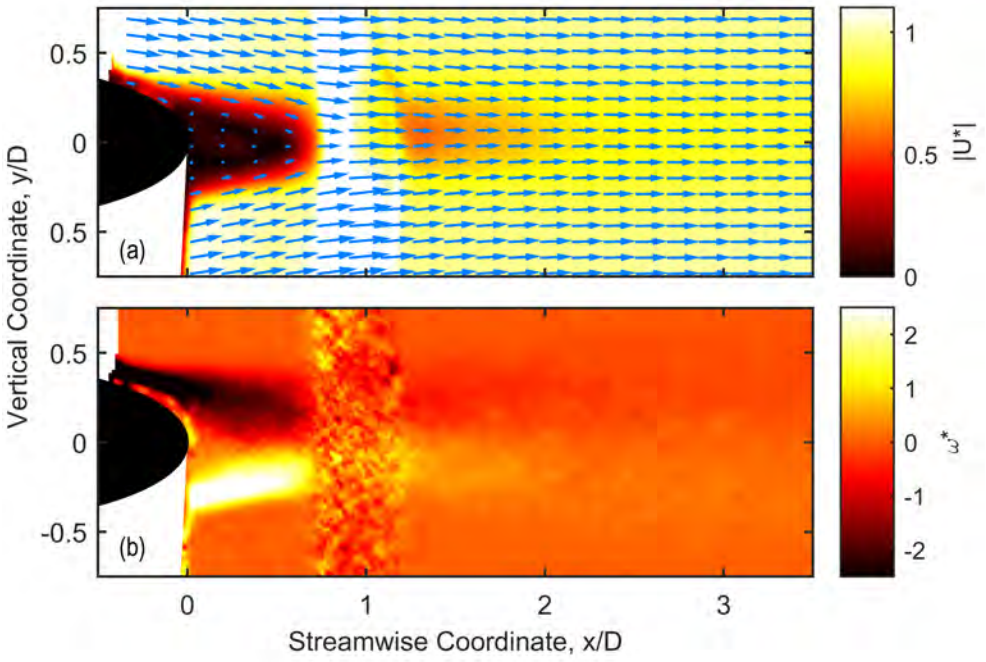

Figure 4.1: Ensemble-averaged baseline (a) velocity field and (b) vorticity ω^*.

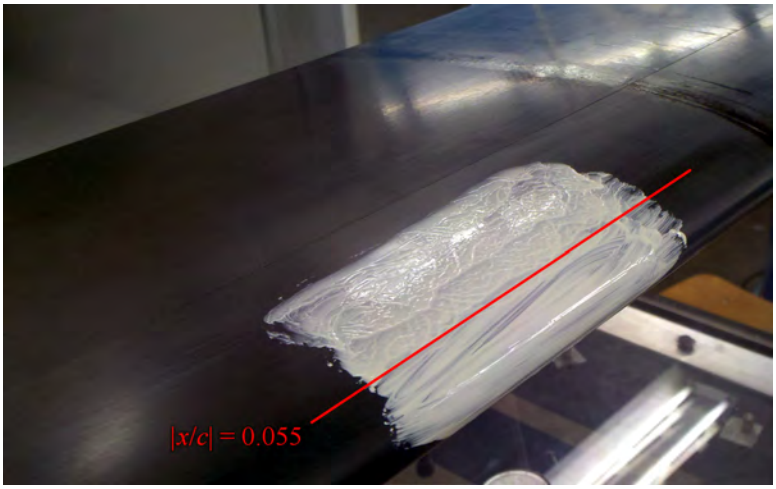

Figure 4.2: Surface oil flow visualization indicating the separation line.

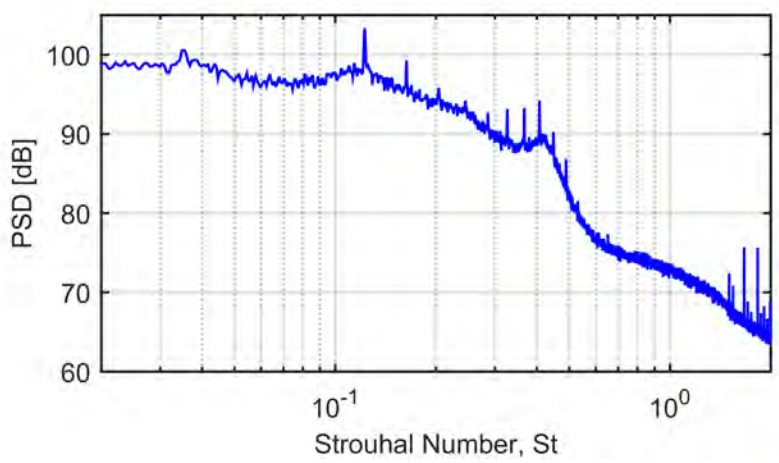

Figure 4.3: Pressure spectrum in the flow just outside of the wake.

hydrodynamic in nature. The baseline pressure spectrum is shown in Fig. 4.3. The fundamental shedding Strouhal number observed in this work is 0.12. The Reynolds number of $5.0 \cdot 10^5$ (or $7.5 \cdot 10^4$ based on equivalent diameter) used in the present experiment corresponds to a transitional regime and the shedding Strouhal number is sensitive to geometry and flow conditions, thus there are significant variations in the shedding Strouhal number found in the literature [19].

A vast sweep of excitation frequencies from $St_F = 0.08$ to 2.25 was performed using a single actuator. However, other than the detection of actuator tones, there was no discernible influence upon the baseline behavior. Thus, the NS-DBDs lack sufficient control authority in this configuration. There are two potential reasons for this inadequacy. The first is due to the lack of momentum addition. In this case, the use of AC-DBDs would be better suited for this task, since they function via body force. In fact, Bhattacharya *et al.* [32–34] have used AC-DBDs successfully to control the wake of a circular cylinder at Reynolds numbers (based on diameter) of up to

$4.0 \cdot 10^4$. Another possibility is that the boundary layer is too thick and turbulent. Ely *et al.* [51, 52] found that NS-DBDs lacked control authority on a free shear layer when the incoming boundary layer thickness was too great. Unlike a circular cylinder, a NACA 0015 in reverse flow has substantial length in the streamwise direction for a boundary layer to form and grow prior to the shear layer formation.

Further optimizations were considered, but not employed. The simultaneous utilization of both actuators could have been practically utilized in one of two manners: in-phase excitation, which would introduce a pinching-like perturbation on the recirculation; and, 180° out-of-phase excitation, which would emphasize the alternating motion of the recirculation and wake. Furthermore, spanwise periodic excitation has been demonstrated to improve the efficacy of unsteady forcing [25, 34]. However, if one of these methods were to exhibit superior control, it is theorized that a single actuator should also exhibit some degree of control. Since no control authority was observed, the exploration of these potential optimizations was unnecessary.

Chapter 5: Fifteen-Degree Angle of Attack

Ensemble-averaged $\alpha = 15°$ baseline PIV images are shown in Fig. 5.1. The circular arc is the edge of an acrylic disk used to mount the airfoil. Two sets of PIV images, one covering the flow over the airfoil and the other the wake region, were obtained. The ensemble-averaged baseline and ALE excitation (ensemble- and phase-averaged) cases have had the velocity fields over the airfoil and in the wake stitched together at $x/D = 0$. The darkest shade in Fig. 5.1(a) represents a velocity magnitude near zero and thus provides a closed contour around separated flow. The separated region on the suction side of the airfoil began just past the ALE and extends well beyond the airfoil. The velocity vectors provide a clear indication of a large recirculation present in the time-averaged sense. Vorticity shown in Fig. 5.1(b) highlights a free shear layer on either end of the airfoil: a long and narrow shear layer from the ALE and a much wider shear layer from the ATE. Both the velocity and the vorticity behind the airfoil were highly asymmetric, similar to those of an inclined flat plate at $Re = 2.0 \cdot 10^4$ and $\alpha = 18°$ [21]. TKE shown in Fig. 5.1(c) was greatest in the ATE shear layer near where the two shear layers meet.

It is important to consider TKE in addition to vorticity. Vorticity highlights regions of high rotation and shear, such as the shear layers on either end of the airfoil. The vorticity is most intense at the center of each shear layer, where both

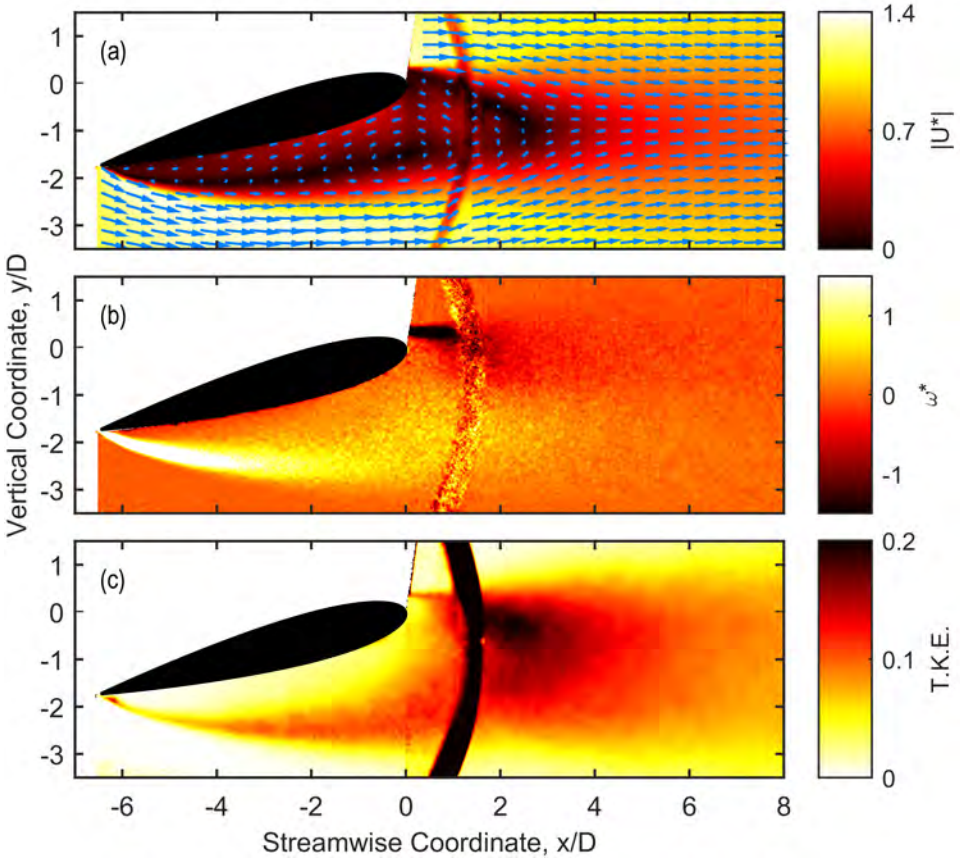

Figure 5.1: Ensemble-averaged baseline (a) velocity field, (b) vorticity ω^*, and (c) turbulent kinetic energy.

rotation and shear are maximum. This is useful for determining the flow topology in a time-averaged sense. TKE highlights dynamic regions of the flow, which elucidates flow interactions that occur naturally or due to excitation. From Fig. 5.1 it is obvious that the shear layers are unsteady, but the greatest interaction was observed where the two shear layers meet. Reducing the separation behind the airfoil should also reduce the unsteadiness observed in this region; this will be discussed further in Section 5.1.

Pressure spectra were obtained to investigate vortex-shedding frequency from both the ALE and ATE. The vorticity map shown in Fig. 5.1(b) was used to determine

suitable microphone locations. Three microphone locations were utilized: one near the ATE shear layer (A) and two near the ALE shear layer (B and C), illustrated in Fig. 3.3. Microphone locations A and B were one airfoil-thickness away (up/down) and one thickness downstream from the ATE and ALE of the airfoil, respectively. Location C was at the same streamwise location as A, but on the opposite side of the wake. Although the microphone was placed outside of the shear layer in each case, the positioning was close enough that the spectra were predominately hydrodynamic in nature. The resultant pressure spectra are shown in Fig. 5.2; note that the spectra are ordered A-C-B. Each spectrum was shifted by 20 dB for clarity. Each horizontal gray line is 110 dB for reference. Spectra obtained at locations A and C are very similar: a large narrowband peak corresponding to the fundamental shedding frequency occurred at $St = 0.19$ with a smaller harmonic at $St = 0.38$. The spectra are nearly uniform below the shedding frequency; above the shedding frequency they decay at 30 dB/decade at location A and 25 dB/decade at location C. Spectra of this nature are typical of bluff body shedding and the natural shedding frequency is close to that observed by Lind *et al.* on a NACA 0012 in reverse flow [24]. The spectrum at location C also has a small peak at $St = 0.33$. The spectrum at location B has the same narrowband peak at the fundamental shedding frequency of $St = 0.19$, but no notable harmonic. Instead, there are small peaks at $St = 0.33$ (similar to that from location C), 0.44, and 0.66. The sources of these peaks are not clear at this time. In addition, there is a broadband peak around $St = 0.07$ that may correspond to unsteady motion of a potential small laminar separation bubble near the ALE [53, 54].

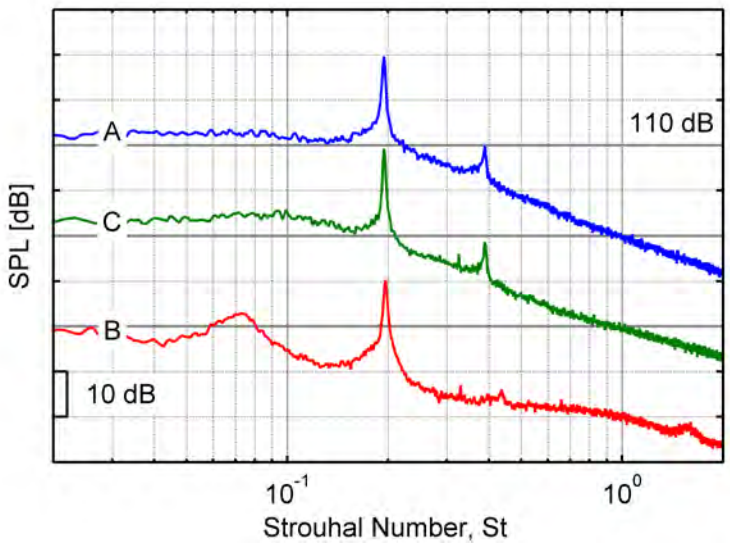

Figure 5.2: Pressure spectra in the flow just outside of the shear layer.

Swirling strength, used for identification of vortices, is shown in Fig. 5.3 for the baseline case. The phase-averaged baseline and ATE excitation cases were captured with a two-camera arrangement that effectively avoids corruption due to the acrylic mounting disk, as detailed in Section 3.6. Vortices from the ATE grew rapidly and synchronize with those from the ALE, creating a von Kármán vortex street in the wake. The vortex street was asymmetric with the vortices from the ALE being weaker and more elongated than those from the ATE due to their added diffusion. Figure 5.3 therefore illustrates the efficacy of the pressure-based phase locking technique by capturing the natural shedding.

Surface pressure distribution is shown in Fig. 5.4 for the baseline case, before the actuators were installed. The crosses represent data that is in the baseline measurement, but is absent from excited cases due to the installation of actuators. The ALE

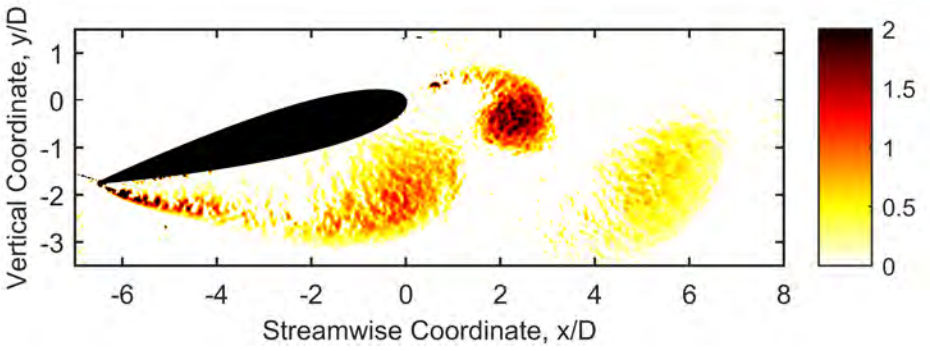

Figure 5.3: Pressure-based phase-averaged swirling strength λ_{ci}^{*} for baseline flow.

actuators did not cover any pressure taps. The presence of the actuators has a negligible impact on the static pressure values (except those taps which are physically covered) due to their low profile construction. On the suction side of the airfoil, the pressure coefficient is relatively constant between $|x/c| = 1.0$ and 0.15, indicating a large separated region. On the pressure side of the airfoil, the pressure coefficient exhibits a linear decrease as the flow accelerates across the ramp-like surface. Near the ATE, the pressure coefficient adjusts as the flow curves around the blunt edge of the airfoil.

The actuators at the ALE and at the ATE may be operated independently. This makes it possible to utilize the actuators individually and even simultaneously. Thus, the following excitation configurations exist: ALE only, ATE only, and simultaneous excitation. Furthermore, simultaneous excitation may be done in one of two manners: the same excitation frequency at either end with a phase delay between (synchronous), or two independent excitation frequencies at either end (asynchronous). These four excitation configurations will be evaluated in the following sections.

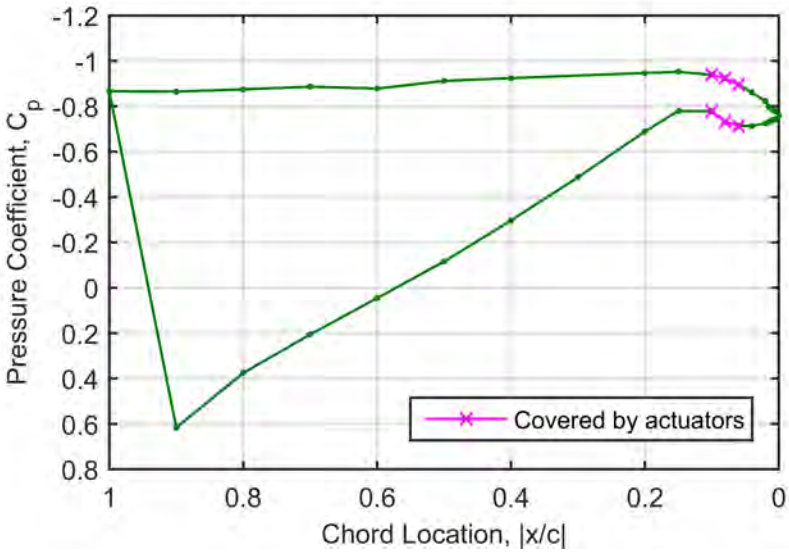

Figure 5.4: Surface pressure distribution on the airfoil for baseline flow.

5.1 Aerodynamic Leading Edge (ALE) Excitation

To evaluate the effect of excitation at the ALE, the suction side actuator near the ALE with electrode junction at $x/c = +0.95$ was utilized. In this configuration, plasma formation occurred just downstream of the shear layer origin.

Excitation was performed using the ALE actuator on the suction side at six excitation Strouhal numbers between $St_F = 0.03$ and 1.08. The ensemble-averaged velocity fields and TKE of each excited case are shown in Fig. 5.5(b–g) and may be compared with the baseline case in Fig. 5.5(a). The fractional change in separation area from baseline for all cases is shown in Fig. 5.6 along with the fractional change in performance metrics which will be discussed later in this section. The following paragraphs will discuss each of these excitation cases in detail.

The velocity field shown in Fig. 5.5(b) for an excitation Strouhal number of $St_F = 0.03$ shows the wake slightly widened and the separation extent decreased. The

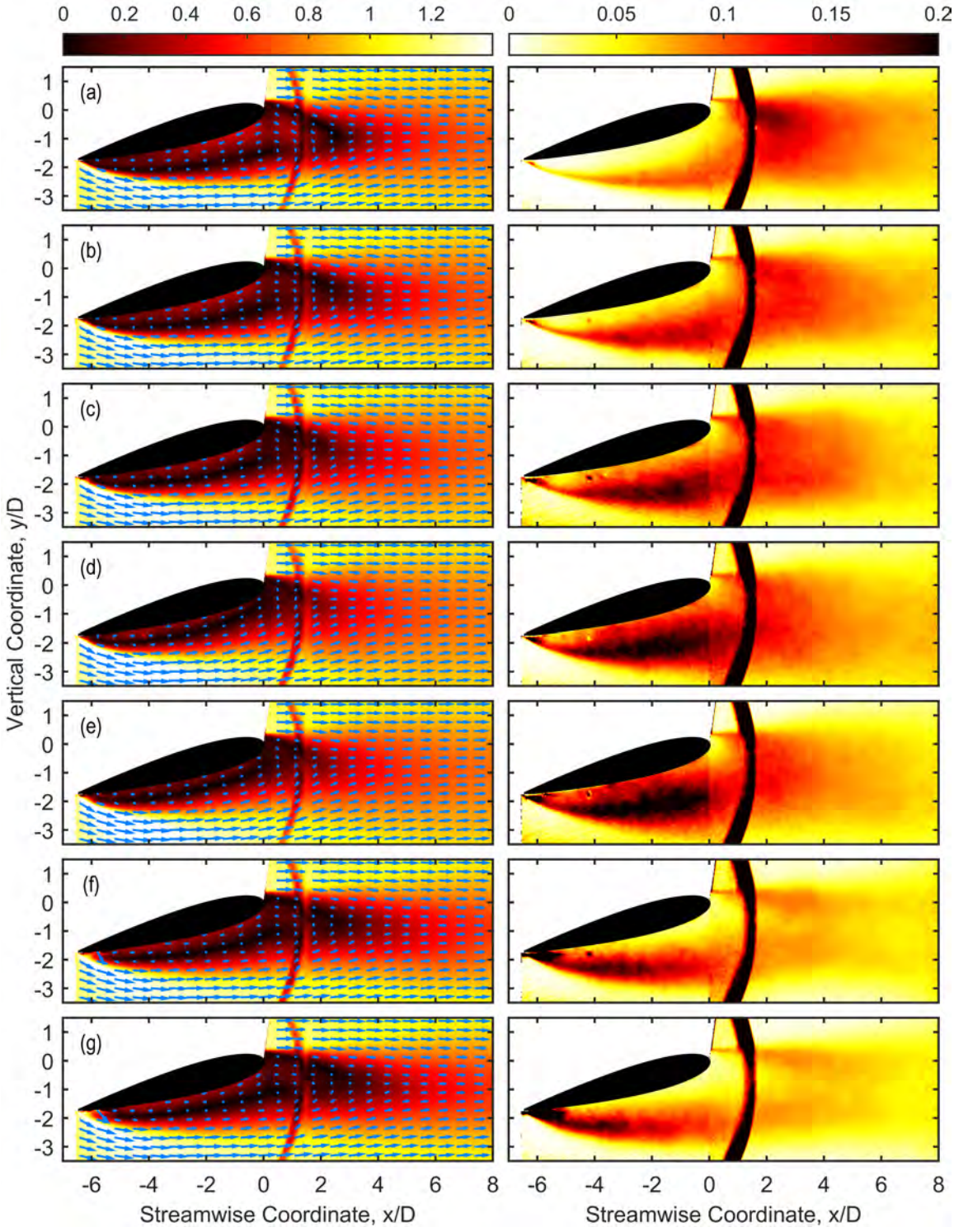

Figure 5.5: Ensemble-averaged velocity field (left) and TKE (right) with ALE excitation of $St_F = 0.00$ [baseline], 0.03, 0.08, 0.15, 0.19, 0.62, and 1.08 from (a) to (g), respectively.

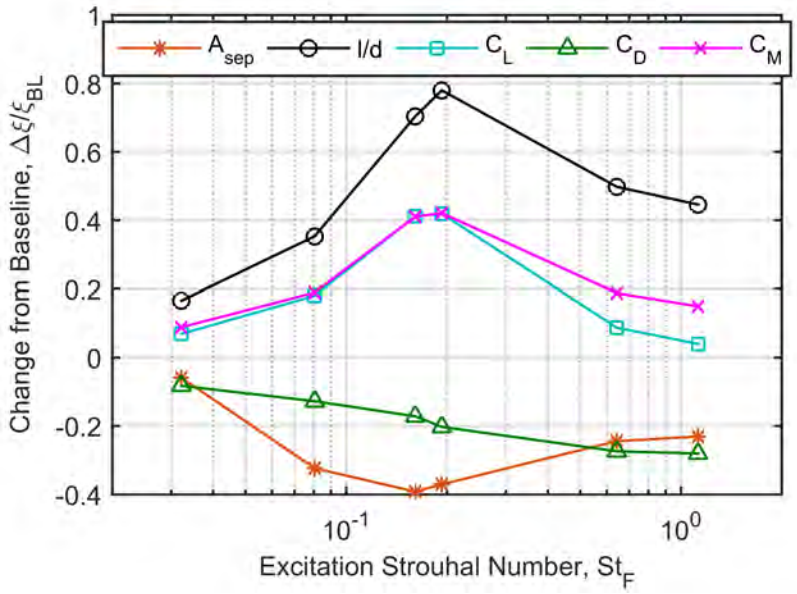

Figure 5.6: Changes in separation area, lift-to-drag ratio, sectional lift, drag, and moment coefficients with ALE excitation.

separation area was reduced by 6% from that of the baseline. TKE was similar in magnitude to that of the baseline, but more uniformly distributed among the shear layers. While these effects were relatively small, they were statistically significant. This is surprising, considering that the excitation Strouhal number in this case is an order of magnitude less than the shedding Strouhal number, and shows that the flow responds to excitation over a large range of excitation frequencies. Note that the time-averaged heating by the actuator was too small to have noticeable influence on the flow. The actuator energy was about 3 mJ per pulse (see Fig. 3.6); this was a time-averaged power of 60 mW for $St_F = 0.03$, or less than 0.01% of the flow power through the test section height of c' (airfoil blockage height). In addition, phase-averaged PIV measurements that will be shown and discussed later will confirm that the flow responded to the excitation.

The velocity field shown in Fig. 5.5(c) for an excitation Strouhal number of $St_F = 0.08$ is similar to that of $St_F = 0.03$. The wake widened slightly more, but the separation area was notably smaller with a 32% reduction from the baseline. The most intense region of TKE shifted to the ALE shear layer, opposite to that of the baseline where TKE was most intense in the ATE shear layer. This suggests that ALE excitation altered the global behavior of the flow field, resulting in dynamic regions different from those which naturally occur. The frequency content of the ALE shear layer will be discussed later.

The velocity fields shown in Fig. 5.5(d–e) correspond to excitation Strouhal numbers of $St_F = 0.15$ and 0.19, respectively. TKE was concentrated in the ALE shear layer with greater magnitude than in the baseline case. Although $St_F = 0.19$ had slightly more intense TKE, $St_F = 0.15$ resulted in the smallest separated region. While the wake widened, the separation extent significantly decreased. The separation region extended only to $x/D = 0.8$ (if corruption due to the acrylic disk is ignored) compared to 2.5 in the baseline case. Furthermore, the separation area was reduced by 39% from baseline. Control near these frequencies excites the shear layer over the separation region making the large-scale structures more coherent and enhancing their entrainment capabilities and thus reducing the separation region but widening the wake, due to increased mixing caused by these structures.

The velocity fields shown in Fig. 5.5(f–g) for excitation Strouhal numbers of $St_F = 0.62$ and 1.08 show the wake widened some and the separation was skewed toward the ATE. The separation was slightly stretched to $x/D = 2.6$ compared to 2.5 in the baseline case and the end of separation moved from $y/D = -0.96$ to -0.61. The separation area was reduced by 23%. Overall, the separation appears more streamlined

(elongated and thin) than the baseline case. TKE was highly concentrated near the ALE with little energy observed in the wake region. This suggests that dynamic content in the wake region was significantly reduced, which will be explored further with phase-locked swirling strength below. Again, the results show that the flow responds to excitation over a large range of excitation frequencies, and since the time-averaged heating power of this case is over 7 times higher than that of the $St_F = 0.15$ case, the effect is clearly due to the excitation of instabilities rather than just heating.

The pressure spectra at locations B and C (see Fig. 3.3) of baseline (annotated 0.00) and excited cases are shown in Fig. 5.7. Each spectrum was shifted by 20 dB for clarity. Probe location B was very near the ALE actuator, whereas location C was farther downstream the same shear layer. Eighteen excitation Strouhal numbers between $St_F = 0.03$ and $\sim$1.90 were tested. Excitation at all moderate excitation frequencies eliminates the fundamental peak (and its harmonic). At location C, excitation at Strouhal numbers between $St_F = 0.03$ and 0.38 display the same broadband characteristics as the baseline case, but with altered peaks. The same is true at location B, except that the broadband peak near $St = 0.07$ is also eliminated. Excitation at $St_F = 0.16$ introduces a broadband peak at $St = 0.08$ visible at location C, which isn't present with excitation at $St_F = 0.08$ nor is it visible at location B. Similarly, excitation from $St_F = 0.19$ to 0.32 increases the **s**ound **p**ressure **l**evel (SPL) over a broad range below the excitation Strouhal number. These are possible indications that unsteady motion of a laminar separation bubble near the ALE had been enhanced; a small drift of the shear layer at low frequencies would exhibit itself as a broadband increase more easily observed far from the shear layer origin. Excitation from $St_F = 0.87$ to 1.89 introduce high-frequency content into the upstream portion

of the shear layer, but this content is not observed at the downstream location. In fact, at $St_F = 1.89$, the downstream spectrum appears similar in nature to the baseline case. This indicates that high-frequency perturbations are not sustainable by the ALE shear layer and decay rapidly as they convect downstream. Since the actuators generate an acoustic tone at the forcing frequency (and its harmonics), it is not clear from these spectra whether the excitations generate shedding at the excitation frequencies or not. This will become clear from the phase-averaged PIV results shown in Fig. 5.8.

Phase-averaged swirling strength images with ALE excitation are shown in Fig. 5.8, gathered using an actuator-based trigger signal. The phase presented here is $\phi = 90°$, because it contains the most clearly identifiable vortex pattern in the wake. The other phases were similar in appearance, with the vortices at different locations in their convective path. All of the ALE excitation cases exhibit coherent structures over the separation with structure size and separation distance between the structures dependent on the excitation Strouhal number. Excitation at low Strouhal numbers ($St_F = 0.03$ and 0.08) created large coherent structures with correspondingly large separation between them. These low Strouhal numbers produced an impulse response: the flow resumed its natural state after approximately 20 ms for the $St_F = 0.03$ case and 10 ms for the $St_F = 0.08$ case. For comparison, the convective time along the chord of the airfoil was approximately 8 ms. Further information on impulse response can be found in Sinha *et al.* [55]. Excitation at moderate Strouhal numbers ($St_F = 0.16$ and 0.19) resulted in moderately sized coherent structures that convected far downstream. For all the above cases, the two shear layers maintained their interlocking synchronization. Excitation at high Strouhal numbers ($St_F = 0.88$ and 1.12) resulted

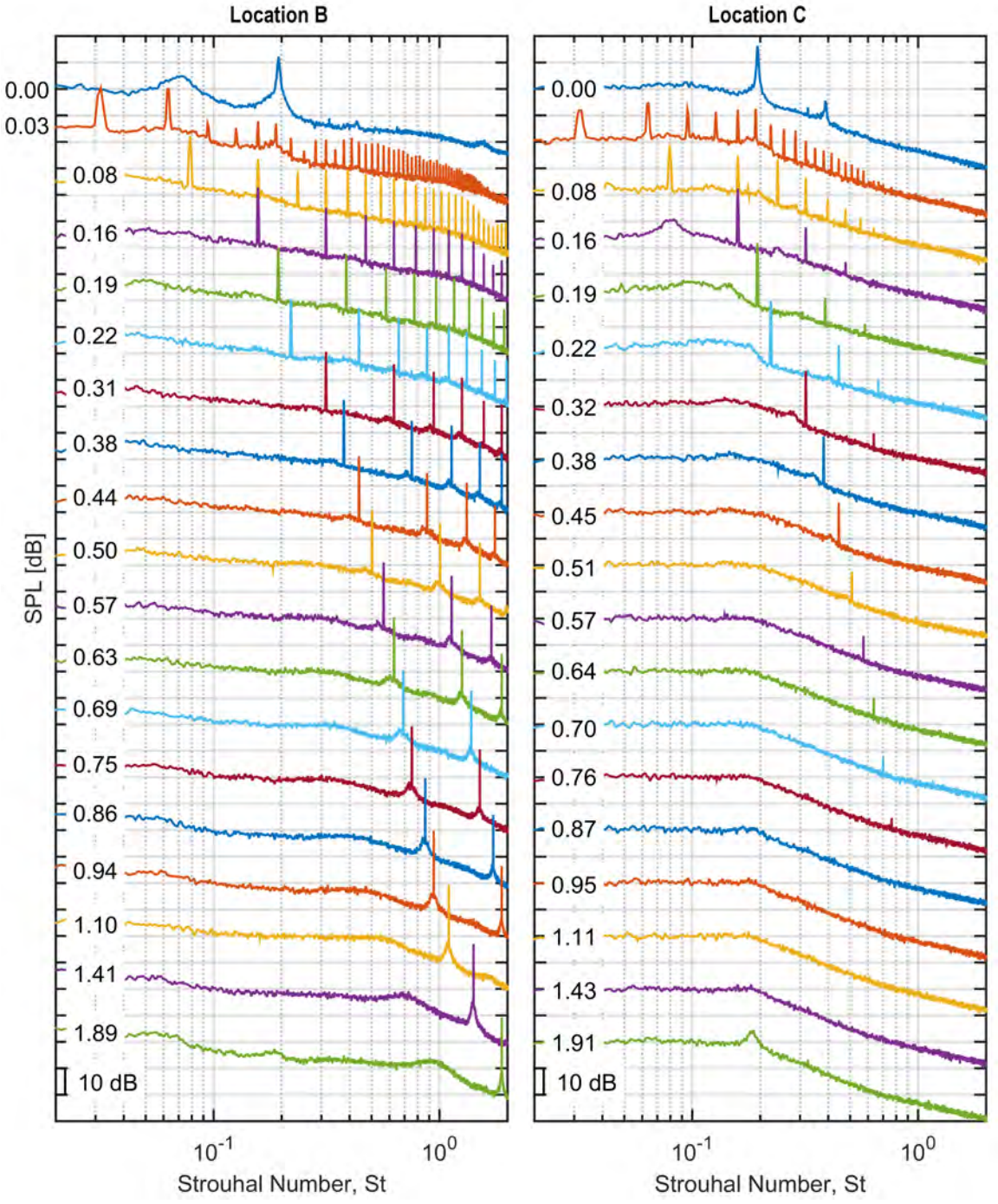

Figure 5.7: Pressure spectra in the wake with ALE excitation captured at locations B and C.

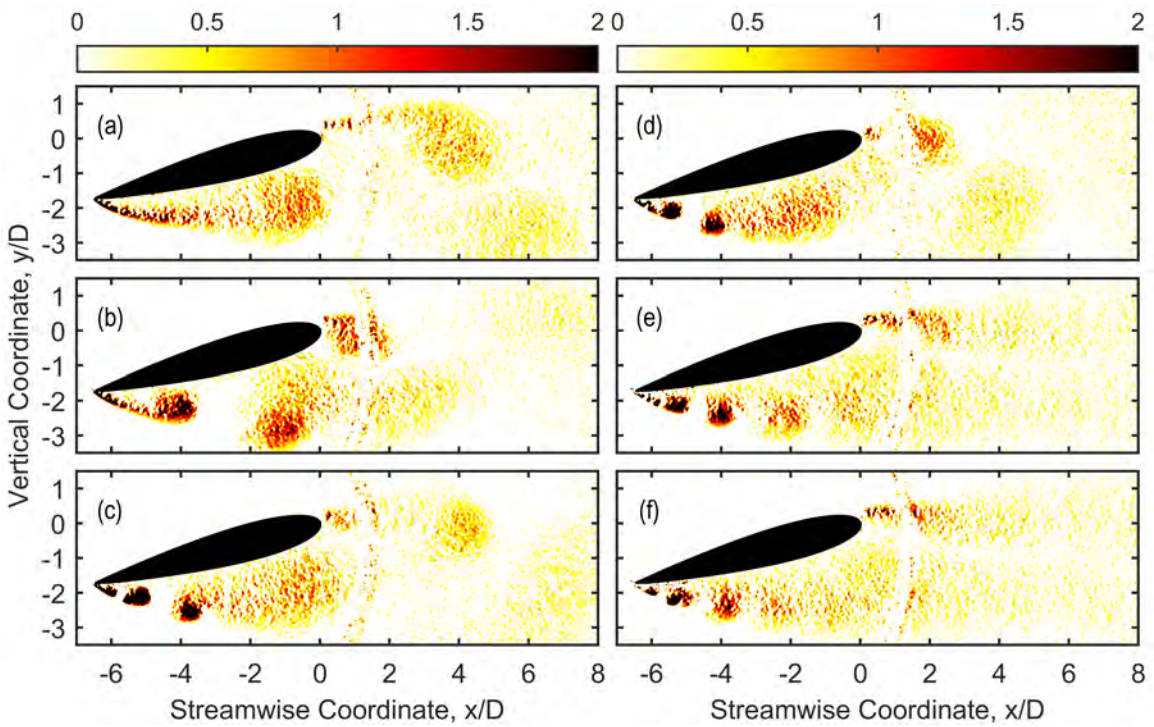

Figure 5.8: Phase-averaged swirling strength λ_{ci}^* with ALE excitation of $St_F = 0.03$, 0.08, 0.16, 0.19, 0.88, and 1.12 from (a) to (f), respectively.

in structures similar in size and separation distance to the moderate excitation, but with no synchronization of the shear layers; these structures appear to quickly diffuse in the wake. The response of the flow to the excitation is strongest when the excitation Strouhal number near the natural shedding Strouhal number of 0.19.

The reason for the similarity of the structures' size and separation distance for the excitation at $St_F = 0.88$ (5 times 0.176) and 1.12 (7 times 0.16) to those of $St_F = 0.19$ or 0.16 is not clear. A detailed view of the ALE shear layer with ALE excitation of $St_F = 0.88$ is provided in Fig. 5.9. Note that the phase in this figure is $\phi = 180°$, rather than 90°, as it had the most clearly identifiable structures near the ALE. From Fig. 5.9 it is evident that many small structures (noted by the blue arrows) originate

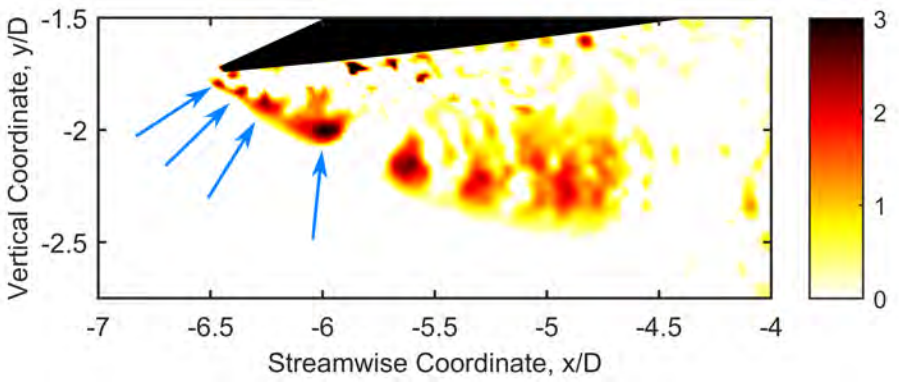

Figure 5.9: Phase-averaged swirling strength λ_{ci}^* detail of ALE shear layer with ALE excitation of $St_F = 0.88$.

from the sharp leading-edge. However, as previously discussed, the structures in the wake region are relatively invariant in size and separation. A plausible explanation is that the shear layer responds to the high-frequency excitation (resulting in many small structures), but the bulk flow cannot respond, and as a result the flow reverts back to its natural shedding state (larger more widely separated structures), but with weaker structures. Indeed, the number of structures observed in Fig. 5.9 from $x/D = -5.7$ to -4.6 is difficult to discern. Perhaps several smaller structures have merged into one or more larger structures, but as a result of merging they are weaker and thus diffuse more rapidly.

These results confirm that the flow responds to the excitation over a large range of excitation Strouhal numbers. Over low to moderate excitation Strouhal numbers, the shedding occurs at the excitation Strouhal number and the size and spacing of the structures is commensurate with the excitation. The coherent structures entrain high-momentum flow into the separation region, reducing it as shown in Figs. 5.5

and 5.6, similar to leading edge excitation done with NS-DBDs on a conventionally oriented airfoil [10, 12, 30, 31].

Surface pressure curves are shown in Fig. 5.10 for the baseline (annotated 0.00) and excited cases. On the pressure side of the airfoil, excitation at $St_F = 0.16$ and 0.19 caused a significant uniform increase in the pressure coefficient, while other excitation Strouhal numbers caused a relatively small change to the pressure coefficient. On the suction side, the peak magnitude of the pressure coefficient increased at all excitation Strouhal numbers. For the baseline case, the suction side pressure coefficient was relatively constant between $|x/c| = 1.0$ and 0.15, indicating a large separated region. Excitation at $St_F = 0.03$ and 0.08 caused a moderate increase in suction amount between $|x/c| = 1.0$ and 0.4, with a similar level decrease between $|x/c| = 0.4$ and 0. Excitation at $St_F = 0.16$ and 0.19 had a similar effect, but with a significant increase in suction. As with the ensemble-averaged PIV data, this suggests that ALE excitation enhances shear layer entrainment, bringing high-momentum fluid into the separation region and reducing its overall size. Excitation at $St_F = 0.64$ and 1.13 caused an increase in the pressure coefficient between $|x/c| = 1.0$ and ~ 0.55, but was followed by a decrease between $|x/c| = 0.55$ and 0. The shape seems to indicate that the separation region has been greatly reduced, but the magnitude suggests that the amount of low-momentum fluid is similar to the baseline. The ensemble-averaged PIV data for this case showed a reduction in separation area by a stretching and thinning of the separated zone.

Lift, drag, and moment coefficients, calculated using Eqns. 3.2–3.4, are shown in Fig. 5.6 alongside the change in separation area. The complete C_p distribution cannot be obtained since the installation of actuators covers some of the static pressure taps

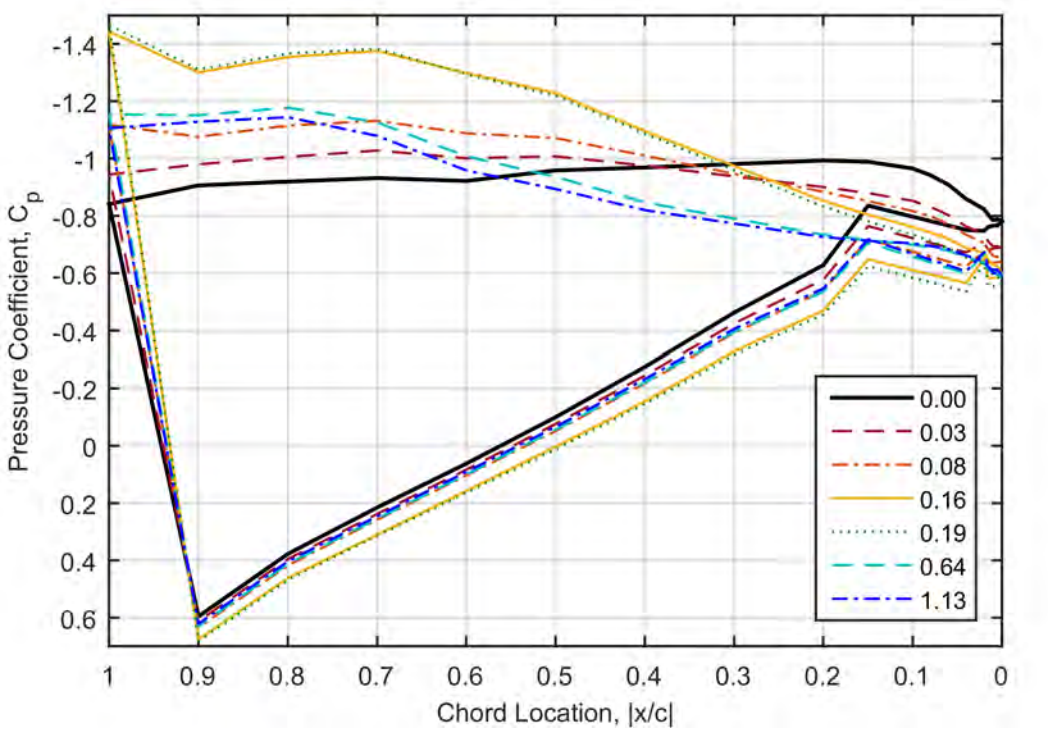

Figure 5.10: Surface pressure distributions over the airfoil with ALE excitation.

(as shown in Fig. 5.4) and the spatial resolution at the ALE is rather poor, since the airfoil was designed to be oriented in the opposite direction; consequently, these measurements serve only as an estimate. All excitation Strouhal numbers decreased the drag coefficient by at least 8%, with the best case ($St_F = 1.13$) decreasing the drag coefficient by 28%. Excitation increased lift at moderate excitation Strouhal numbers, with the best case ($St_F = 0.19$) increasing lift by 42%. At either extreme, excitation increased the lift coefficient by a minimal amount. If this were a typical case, the best excitation Strouhal number would be near $St_F = 0.19$, which would increase the lift by 42% and reduce the drag by 20%. However, in the current orientation of the airfoil, which is representative of a rotor on the in-board portion of the retreating

blade side as portrayed in Fig. 3.3), lift is actually a downward force. In this instance, it is desirable to minimize the lift and drag; thus, excitation near $St_F = 1.13$ would result in a minimal increase in "lift" (by about 4%) and a significant decrease in drag (by about 28%). However, in some other application, it may be desirable to increase lift and thus excite the flow near $St_F = 0.19$.

In summary, plasma actuation at the ALE generated organized coherent structures in the shear layer over the separated region, which convected into the wake region and caused a slight widening of the wake and a reduction of the separation area. Excitation around $St_F = 0.19$, the natural shedding frequency, had the most significant effects: creating moderately sized structures that convected far downstream, reducing the separation area by 37%, increasing lift by 42%, and decreasing drag by 20%. Excitation at much higher Strouhal numbers resulted in the flow returning to its natural shedding state, but with less coherent structures that diffused in the wake, elongating the wake slightly and skewing it toward the ATE. This reduced the separation area and significantly reduced drag. With excitation at the ALE, large-scale structures in the shear layer over the separated zone become more coherent with increased entrainment abilities to bring high-momentum fluid into the separation region; thus reducing the separation region and affecting the lift and drag.

5.2 Aerodynamic Trailing Edge (ATE) Excitation

The interest in ATE excitation is driven primarily by actuator placement: the ATE actuator approximately corresponds with the placement of a leading-edge actuator on a conventionally oriented airfoil. Thus an actuator at this location could provide leading-edge excitation on the advancing blade side and trailing-edge excitation on

the retreating blade side. In addition, Breuer and Jovičić [21] found that the flow past an inclined flat plate was strongly dominated by the behavior of the trailing-edge vortex. Thus, adequate control of the trailing-edge vortex would influence the entire flow field. To evaluate the effect of excitation at the ATE, the pressure side actuator near the ATE with electrode junction at $x/c = -0.07$ was utilized. In this configuration, plasma formation occurred just upstream of the separation line.

Excitation was performed using the ATE actuator on the pressure side at seven excitation Strouhal numbers from $St_F = 0.03$ to 1.28. The ensemble-averaged velocity fields of each excited case are shown in Fig. 5.11(b–h) with TKE similarly shown in Fig. 5.12(b–h). All ATE excited cases used a two-camera PIV setup that allowed for the simultaneous capture of the flow near the airfoil and in the wake region, without the obstruction of the acrylic mounting disk; the two vector fields (one from each camera) were seamlessly blended using DaVis software before any averaging was performed. Each excited case may be compared with the baseline case in the respective subfigure (a). The fractional change in separation area from baseline for all cases is shown in Fig. 5.6 along with the fractional change in performance metrics which will be discussed later in this section. The following paragraphs will discuss each of these excitation cases in detail.

At low excitation Strouhal numbers ($St_F = 0.03$ and 0.08), the wake widened slightly and the separation extent increased; while both effects were relatively small, they were statistically significant. The TKE is very similar to the baseline case, although it is slightly less intense for $St_F = 0.08$. As with the ALE excitation, this demonstrates that the actuators function via excitation of natural flow instabilities even at low excitation frequencies, rather than simple heat addition.

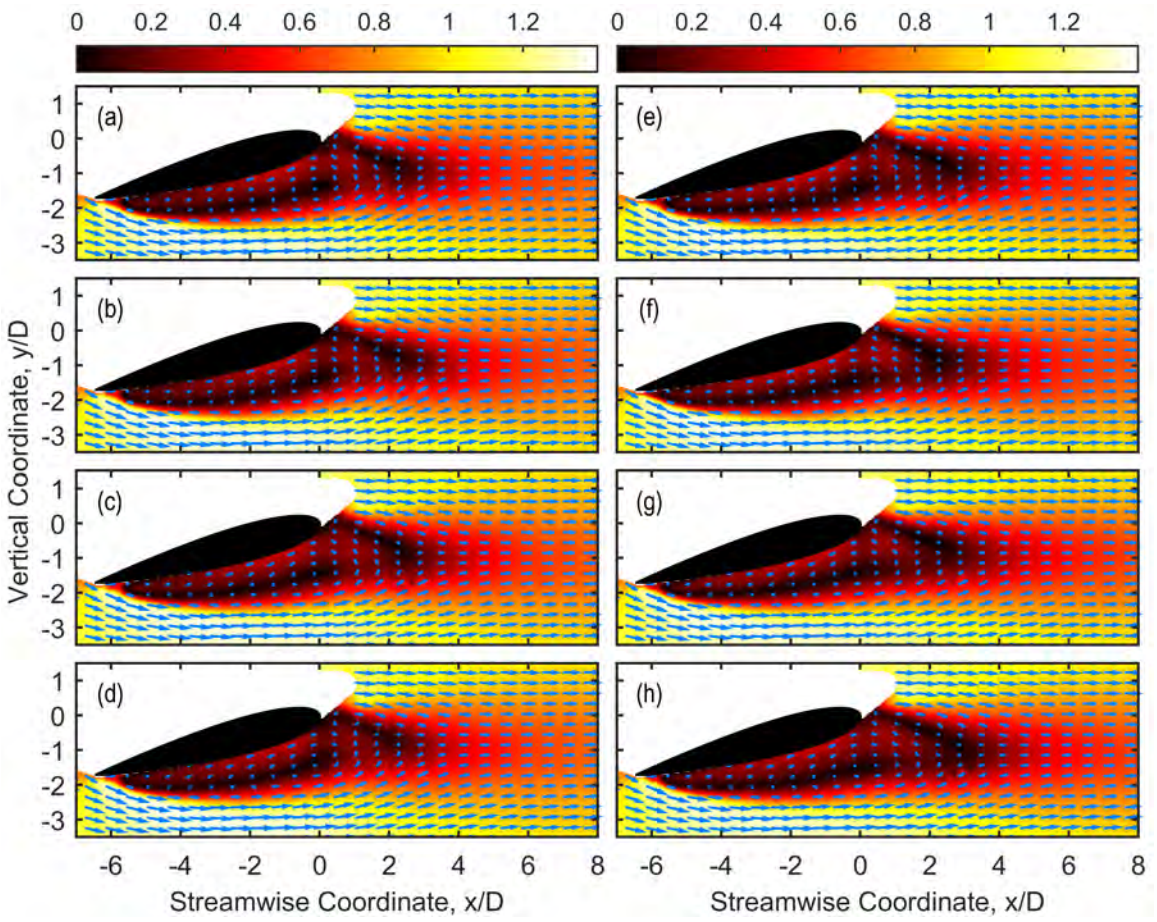

Figure 5.11: Ensemble-averaged velocity field with ATE excitation of St_F = 0.00 [baseline], 0.03, 0.08, 0.19, 0.29, 0.48, 0.64, and 1.28 from (a) to (h), respectively.

Excitation at a Strouhal number of $St_F = 0.19$ had a modest effect, although it was the most significant of the ATE excited cases. The separation region extended to $x/D = 1.8$ compared to 2.3 in the baseline case and the separation area was reduced by 4% from that of the baseline. The TKE intensity is almost identical to the baseline case, with one exception: the region of most intense TKE is smaller in the excited case than in the baseline. This could possibly indicate that the ATE vortex shedding cycle has been refined and exhibits less variation from cycle to cycle.

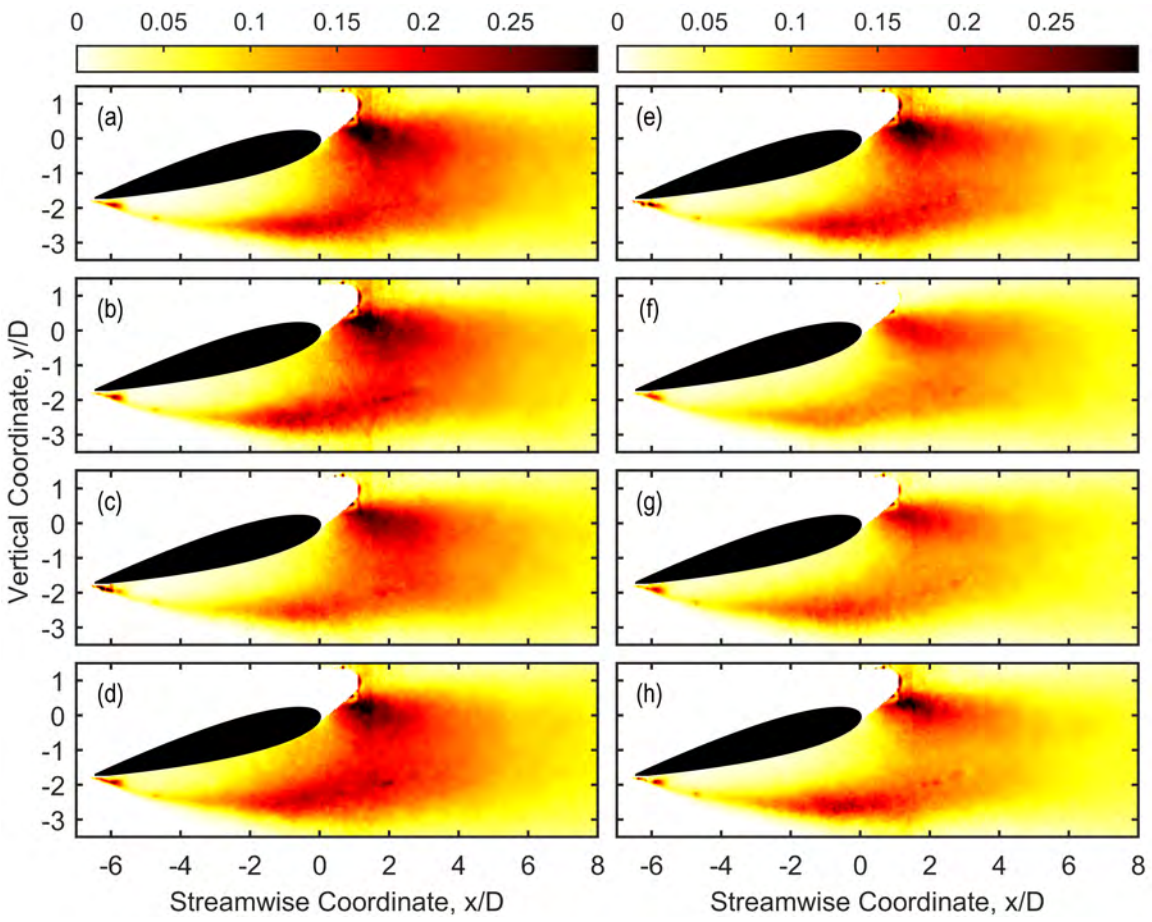

Figure 5.12: Ensemble-averaged TKE with ATE excitation of $St_F = 0.00$ [baseline], 0.03, 0.08, 0.19, 0.29, 0.48, 0.64, and 1.28 from (a) to (h), respectively.

The refinement of the baseline case with $St = 0.19$ ATE excitation will be elaborated upon with pressure spectra and phase-averaged swirling strength later.

Excitation at $St_F = 0.29$ had minimal effect on the flow field. As with the low excitation Strouhal numbers, the wake widened slightly and the separation extent increased. There was a 8% increase in the separation area as compared to the baseline. Although they will be discussed in further detail later, the changes in performance metrics shown in Fig. 5.13 were similarly small for this case.

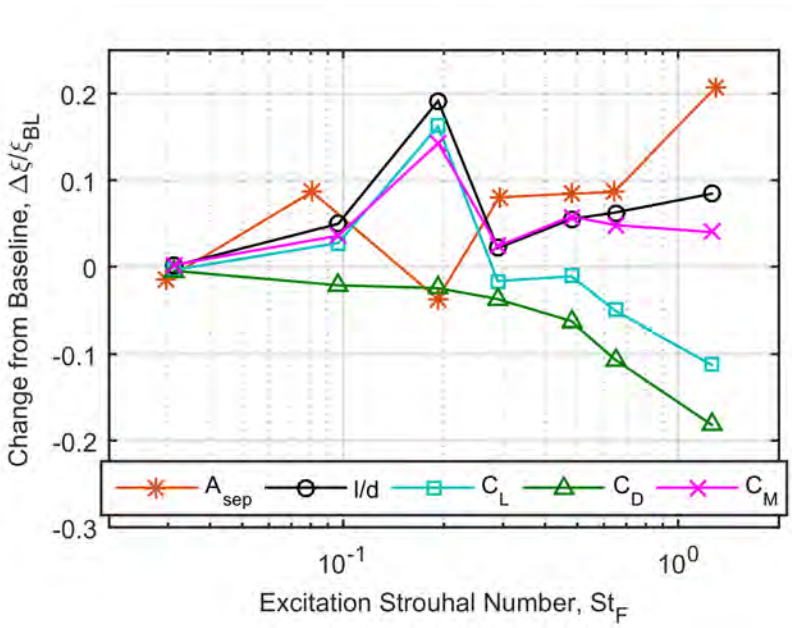

Figure 5.13: Changes in separation area, lift-to-drag ratio, sectional lift, drag, and moment coefficients with ATE excitation.

Excitation at $St_F = 0.48$ widened the wake and extended separation more-so than the previous cases, with a total increase in separation area of 8.5%. Unlike the previous cases, TKE is notably different from the baseline. Although it retains the same general shape and relative intensities, the overall intensity is much less than the baseline. This indicates a large reduction in dynamic content.

At high excitation Strouhal numbers ($St_F = 0.64$ and 1.28), the wake region became wider with lower momentum near the center, indicating reduced mixing. At $St_F = 1.28$, the separation extended to $x/D = 2.9$ compared to 2.3 in the baseline and the separation area was increased by 21% from the baseline. TKE intensity at these excitation frequencies is significantly different from the baseline: the overall intensity is less than the baseline and there are two distinct regions of TKE, one in

each shear layer. The separation of TKE suggests that the interaction of the shear layers has been significantly reduced.

The pressure spectra at locations A and C (see Fig. 3.3) of baseline (annotated 0.00) and forced cases are shown in Fig. 5.14. Each spectrum was shifted by 20 dB for clarity. Probe location A was very near the ATE actuator and location C was on the opposite side of the wake. Fifteen excitation Strouhal numbers between $St_F = 0.03$ and 2.87 were tested. In the baseline case, the dominant peak was at $St = 0.19$ with a harmonic at $St = 0.38$. The actuator tone and the natural shedding at $St = 0.19$ appear in all excited cases, but with smaller and wider shedding peak at higher excitation Strouhal numbers. This indicates that the time between shedding events had greater variance with high frequency ATE excitation. At higher frequencies, there is also less agreement between spectra at locations A and C. For example, excitation at $St_F = 1.28$ appears similar to the baseline at location A, although with reduced peak magnitude, but at location C the peak is nearly eliminated. Recall that these probe locations were at the same streamwise coordinate. Thus, high frequency excitation has the effect of desynchronizing the shear layers. Opposite to high excitation Strouhal numbers, $St_F = 0.19$ produces a spectrum similar to that of the baseline but with a narrow shedding peak; this indicates that the time between shedding events had much less variance and therefore represents a refined baseline. At the highest excitation Strouhal numbers ($St_F = 1.60$ to 2.87), spectra at both locations resemble the baseline case indicating a lack of response from the flow.

Phase-averaged swirling strength is shown in Fig. 5.15 for excitation Strouhal numbers between $St_F = 0.03$ and 1.28, gathered using an actuator-based trigger signal. Note that Fig. 5.15(a) was intentionally left blank, since the baseline cannot be

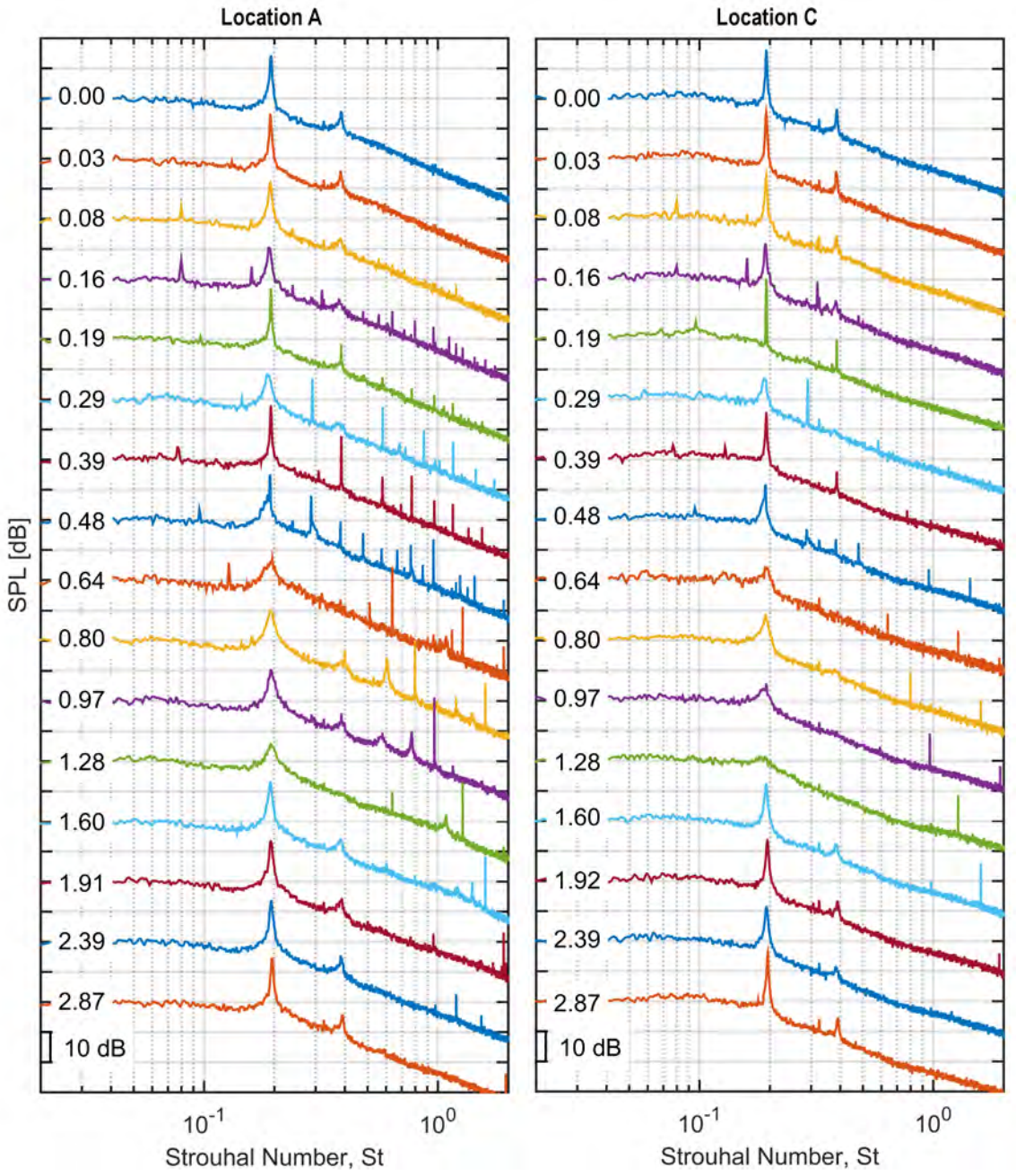

Figure 5.14: Pressure spectra in the wake with ATE excitation captured at locations A and C.

acquired with an actuator-based trigger signal. The phase presented here is $\phi = 90°$. Despite the ATE location of the plasma excitation, there was clearly an influence upon the formation of the structures in the upstream shear layer over the separated region: as the excitation frequency increased, the structures in the shear layer over the separated region became more closely spaced, which means the natural shedding process was modified. With an excitation frequency greater than the natural shedding frequency, there was a loss of phase information in the wake region, making it impossible to discern structures in the wake. Spectral results in Fig. 5.14 indicate that pressure fluctuations in the wake region remain dominated by the natural shedding frequency.

To observe the vorticity in the wake, the PIV system was synchronized with the natural structure shedding. In the first attempt, the microphone at location A in Fig. 3.3 was used for this phase-locking. Pressure fluctuations were acquired and translated into trigger signals in real-time. Due to the large-amplitude acoustic tone from the nearby actuators relative to that of the signal from natural structures, the pressure signal was adversely affected by excitation despite the use of a bandpass filter. Therefore, the microphone was repositioned at location B in Fig. 3.3. Due to the sensitivity of the pressure-based phase locking technique, a conditional average was employed to filter out spurious trigger events.

Swirling strength images with ATE excitation are shown in Fig. 5.16. Figure 5.16(d) shows the image for an excitation Strouhal number of $St_F = 0.19$, which matched the natural shedding Strouhal number. Compared with the baseline case, the vortices were nearly identical in size and location, but were slightly stronger; this agrees with the shedding refinement observed in the spectra of Fig. 5.14. As the excitation

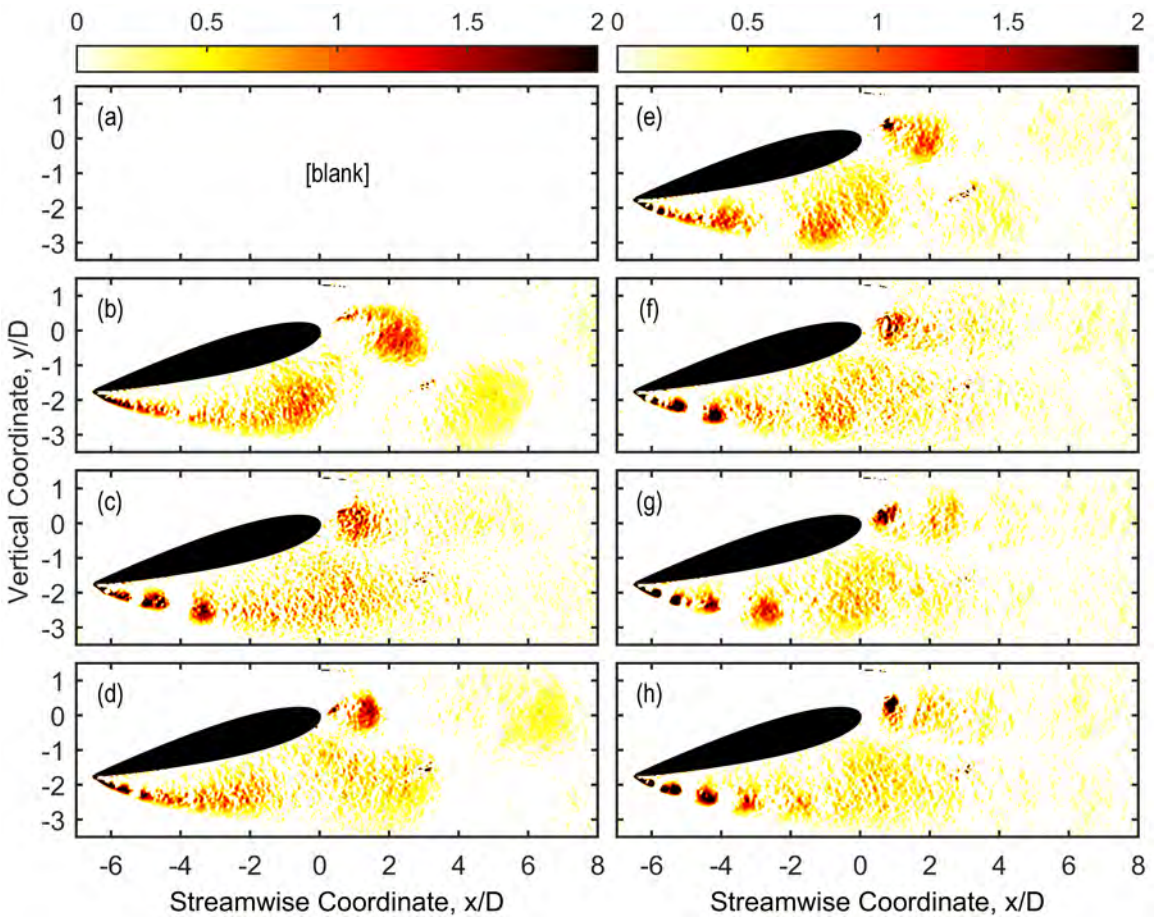

Figure 5.15: Actuator-based phase-averaged swirling strength λ_{ci}^{*} with ATE excitation of $St_F = 0.03$, 0.08, 0.19, 0.29, 0.49, 0.65, and 1.30 from (b) to (h), respectively.

Strouhal number increased, there were two major changes that occurred in the swirling strength. The large structure over the separated region lost coherence, becoming less intense, indicating a loss of phase information. This corresponds to the alteration of the ALE shear layer observed in Fig. 5.15. In the wake, the structures maintained their relative size and location, but were less intense. These results indicate that ATE excitation at the natural shedding frequency reinforced the natural shedding, whereas ATE excitation at frequencies higher than the natural shedding frequency disrupted the natural shedding process, weakening the naturally shed structures.

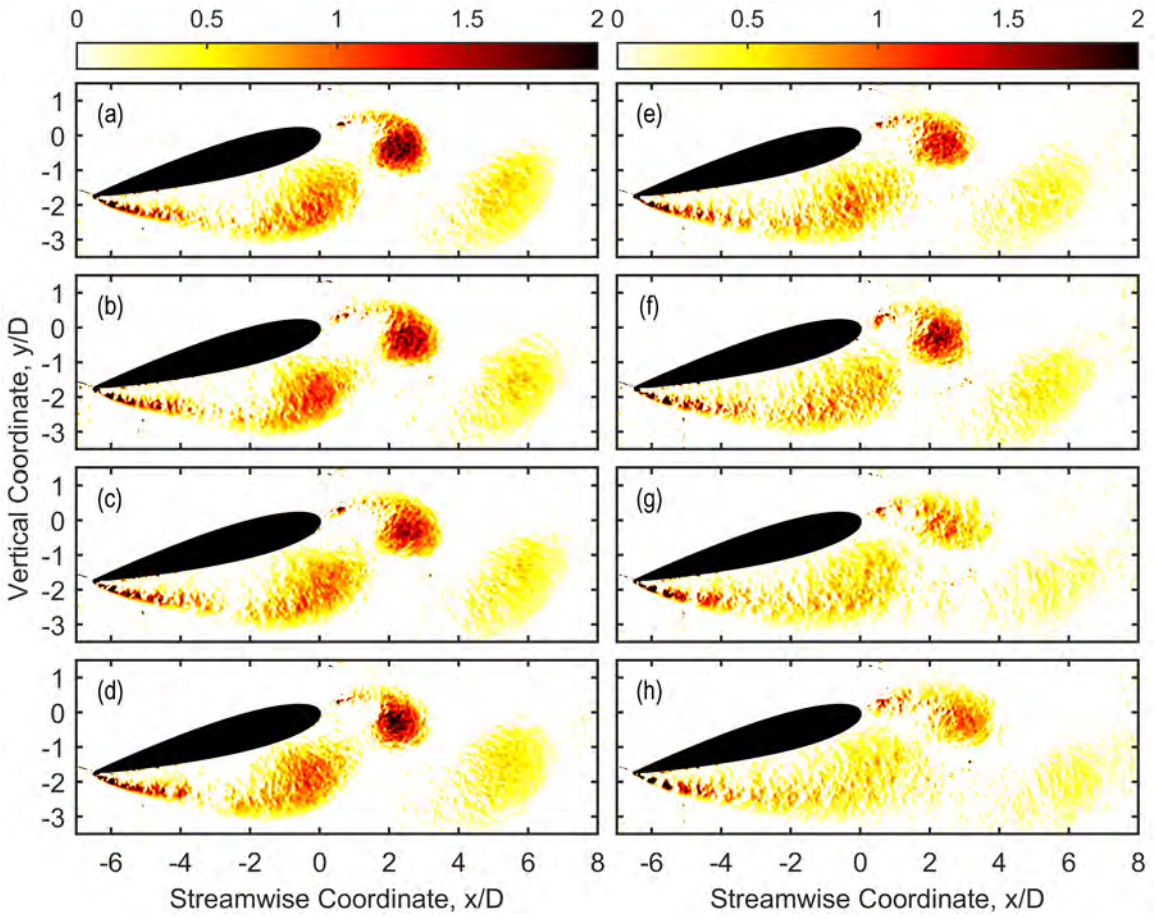

Figure 5.16: Pressure-based phase-averaged swirling strength λ_{ci}^{*} with ATE excitation of $St_F = 0.00$ [baseline], 0.03, 0.08, 0.19, 0.29, 0.48, 0.65, and 1.30 from (a) to (h), respectively.

Surface pressure curves are shown in Fig. 5.17 for the baseline (annotated 0.00) and excited cases. On the pressure side of the airfoil, excitation at $St_F = 0.19$ caused a relatively small but uniform increase in the pressure coefficient, similar to $St_F = 0.16$ and 0.19 in Fig. 5.10. The other excitation Strouhal numbers decreased the pressure coefficient on the pressure side by a marginal amount. On the suction side, excitation altered both the magnitude and shape of the pressure coefficient. For the baseline case, the suction side pressure coefficient was relatively constant

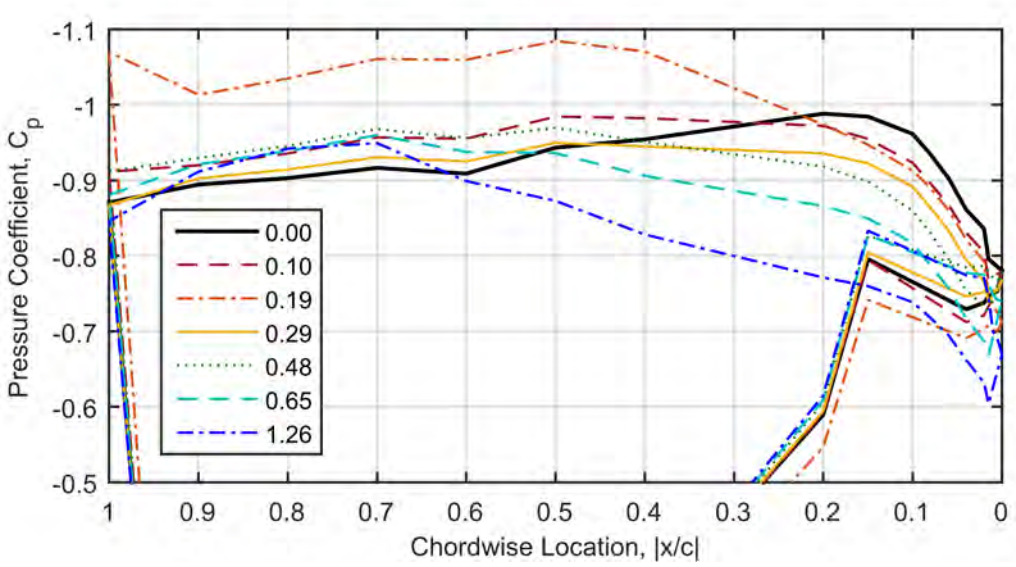

Figure 5.17: Surface pressure distributions with ATE excitation.

between $|x/c| = 1.0$ and 0.15, indicating a large separated region. Excitation at $St_F = 0.19$ increased suction between $|x/c| = 1.0$ and 0.22 with a small decrease thereafter. Excitation at $St_F = 0.10$ had a similar behavior, but the increase in suction was less significant. Excitation at $St_F = 0.48$ resulted in a moderate increase in suction from $|x/c| = 1.0$ to 0.4, with a moderate decrease from $|x/c| = 0.4$ to 0. This is very similar to the ALE excitation of $St_F = 0.03$, except that there was sufficient decrease in suction near the ATE ($|x/c| = 0$) that there was a small region where the suction side pressure was greater than that on the pressure side, resulting in a pressure inversion from $|x/c| = 0.06$ to 0. At higher excitation Strouhal numbers, the decrease in suction was more pronounced, resulting in an even larger region of inversed pressure. Excitation at $St_F = 1.26$ was the most severe: the decrease in pressure began at $|x/c| = 0.62$ and the pressure inversion began at $|x/c| = 0.17$.

In summary, plasma actuation at the ATE caused a reduction in the magnitude of the fundamental and harmonic peaks in pressure spectra over a broad range of excitation Strouhal number. Phase-locked PIV was acquired using both plasma actuation and structure shedding as a trigger event. Phase-locked data in the baseline case was acquired using a filtered pressure signal as a trigger, showing a clearly visible von Kármán vortex street. Excitation at the ATE altered the structures over the separated region, suggesting an upstream communication in the separated region. At excitation frequencies higher than the natural shedding frequency, the natural shedding process was disrupted, weakening the naturally shed structures in the wake.

5.3 Simultaneous Excitation of ALE and ATE

The previous two sections explored the use of plasma excitation at either the ALE or the ATE. Both demonstrated control authority, but the use of ALE excitation was found to have superior control. Although highly asymmetric, the flow behavior at angle of attack is still that of a bluff body. Therefore, it is reasonable to assume that excitation on both sides of the bluff body would exhibit improved efficacy. In theory, the addition of ATE excitation could improve the performance of the already observed ALE excitation. Thus investigating simultaneous excitation will further elucidate the feedback mechanism in the wake region.

Simultaneous excitation was achieved by utilizing actuators with electrode junctions at $x/c = -0.07$ and $+0.95$ simultaneously. The plasma discharges were calibrated such that the peak power of each actuator was approximately equal whether run independently or simultaneously.

5.3.1 Synchronous Excitation

Synchronous operation, where both actuators utilize the same excitation frequency with some phase delay between, is explored here. The optimal phase delay is expected to be such that ATE excitation is out-of-phase with passing ALE structures. In other words, as structures from the ALE convect past the ATE, the ATE actuator would cause an ATE structure to shed between the ALE structures, thus reinforcing the shear layer synchronization. So the delay would be 180° (for out-of-phase) plus a phase-correction corresponding to the convective time between ALE and ATE. The convective time of the shear layer over the separated region is approximately 8 ms. For example, the optimal phase delay for an excitation of 100 Hz is expected to be near $180° + (8 \cdot 10^{-3}\text{s})\,(360° \cdot 100\text{s}^{-1}) = 468°$ or equivalently 108°. This assumes that the ATE excitation will reinforce the effects of ALE excitation. However, it neglects the fact that ATE forcing, on its own, appears to influence the shear layer over the separated region. It is possible that the optimal phase delay corresponds to a synchronous effect at the ALE, where (after an acoustic delay) the ATE excitation strengthens the ALE excitation. If that is the case, the optimal phase delay would be near zero, since the acoustic timescale is significantly less than that of the convective timescale.

Pressure spectra were gathered at location C as an exploratory measure for simultaneous excitation. A multitude of excitation Strouhal numbers and phase delays were explored, but in almost all cases the ALE excitation dominated and the addition ATE excitation was negligible. However, there were two exceptions: $St_F = 0.16$ with $\phi_{ATE} \sim 135°$, and $St_F = 0.89$ with $\phi_{ATE} \sim 155°$. In both cases, the optimal (*i.e.* most distinct from ALE only) phase sensitivity was $\pm 10°$. Estimating the phase

corresponding to constructive interference results in 108° for $St_F = 0.16$ (∼100 Hz) and 144° for $St_F = 0.89$ (∼550 Hz). Therefore it is likely that constructive interference is occurring. Why the other frequencies did not exhibit similar behavior is unknown at this time.

Pressure spectra at location C (illustrated in Fig. 3.3) are shown in Fig. 5.18 for the baseline case and excitation Strouhal numbers of 0.16 and 0.89. Each spectrum was shifted by 20 dB for clarity and paired with a baseline in gray for reference. In the baseline case, the dominant peak was at $St_F = 0.19$ with a harmonic at $St_F = 0.38$. For an excitation Strouhal number of 0.16, shown in Fig. 5.18(a), ALE excitation displaced the natural shedding and its harmonic to 0.16 and 0.32, respectively, and created additional broadband peaks at Strouhal numbers of 0.08 and 0.24. In addition, there was an almost uniform increase in SPL over all Strouhal numbers. ATE excitation at $St_F = 0.16$ reduced the magnitude of the natural shedding peak and its harmonic and introduced actuator tones at Strouhal numbers of 0.16 and 0.32. Combining both ALE and ATE excitation with a phase difference of $\phi_{ATE} = 135°$ again displaced the natural shedding and its harmonic to 0.16 and 0.32, respectively. In addition, there was an overall increase in SPL, though of lesser magnitude than the ALE only case. Broadband peaks at Strouhal numbers at 0.08 and 0.24 may be present, but are difficult to distinguish from the overall increase. For an excitation Strouhal number of 0.88, shown in Fig. 5.18(b), ALE excitation caused a slight but uniform increase in SPL from $St = 0.10$ and up, but otherwise there are no discerning features such as natural shedding peaks or actuator tones. ATE excitation at $St_F = 0.88$ significantly reduced the magnitude of the natural shedding peak and eliminated the

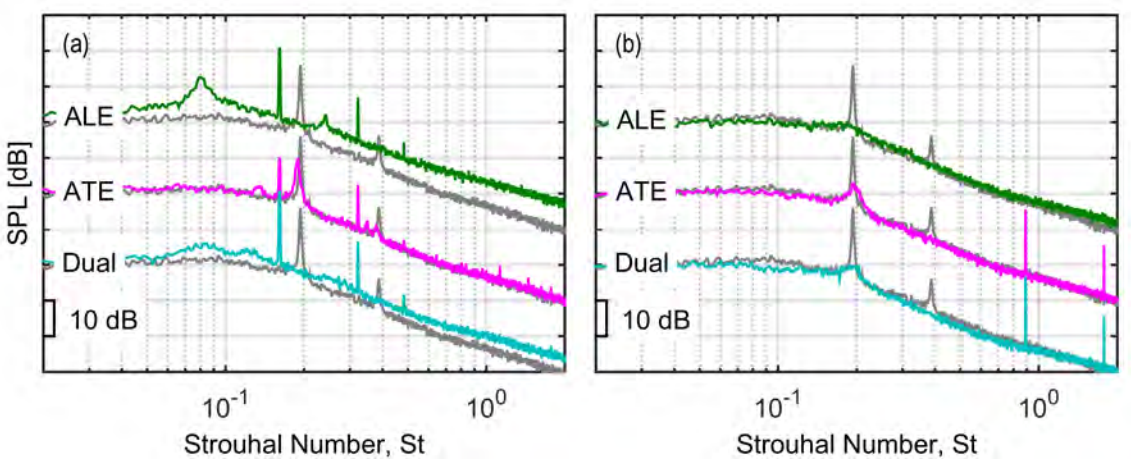

Figure 5.18: Pressure spectra at location C with (a) $St_F = 0.16$ and (b) $St_F = 0.89$, where ϕ_{ATE} for the synchronous excitation cases were 135° and 155°, respectively.

harmonic; actuator tones at Strouhal numbers of 0.88 and 1.76 are visible. Combining both ALE and ATE excitation with a phase difference of $\phi_{ATE} = 155°$ resembles ATE only excitation, except that the magnitude of the natural shedding peak has decreased further and there is a slight decrease in SPL between $St_F = 0.07$ and 1.0.

Static pressure curves are shown in Fig. 5.19 for the baseline case and excitation Strouhal numbers of 0.16 and 0.89. Note that the y-axes differ in scale. In the baseline case, the suction-side pressure coefficient was relatively constant between $|x/c| = 1.0$ and 0.15, indicating a large separated region. For an excitation Strouhal number of 0.16, shown in Fig. 5.19(a), ALE excitation caused a uniform increase in pressure on the pressure-side and a significant increase in suction between $|x/c| = 1.0$ and 0.3 with decrease in suction thereafter. ATE excitation at $St_F = 0.16$ decreased suction slightly near the ATE, but otherwise had a minimal impact on the static pressure profile. Combining both ALE and ATE excitation with a phase difference of $\phi_{ATE} = 135°$ mostly resembles the ALE only case, but with moderate reduction in both pressure

	$St_F = 0.16$			$St_F = 0.89$		
Metric	ALE	ATE	Both	ALE	ATE	Both
l/d	+73	+1.6	+51	+32	+3.3	+9.8
C_L	+47	-2.0	+31	+3.5	-10	-8.0
C_D	-15	-3.6	-13	-21	-13	-16
C_M	+46	+0.45	+32	+11	+1.2	+5.1

Table 5.1: Change in performance metrics (%) with synchronous excitation.

and suction. For an excitation Strouhal number of 0.89, shown in Fig. 5.19(b), ALE excitation caused a uniform increase in pressure on the pressure-side and moderate increase in suction between $|x/c| = 1.0$ and 0.52, but was followed by a decrease between $|x/c| = 0.52$ and 0. ATE excitation at $St_F = 0.89$ decreased suction significantly near the ATE, causing the suction-side pressure to be greater than that on the pressure-side, resulting in a pressure inversion from $|x/c| = 0.16$ to 0. Combining both ALE and ATE excitation with a phase difference of $\phi_{ATE} = 155^\circ$ had a slight suction increase near the ALE, similar to ALE only excitation, but was not accompanied by the uniform increase in pressure on the pressure-side; the combined excitation also mimiced the reduction in pressure near the ATE and pressure inversion of the ATE only case. The influence of these two excitation cases on standard performance metrics is summarized in Table 5.1. For both excitation Strouhal numbers, the static pressure profile and all four performance metrics of the combined excitation lies somewhere between the independent excitation cases. Although the time scale associated with the phase delays was approximately equal to that corresponding to constructive interference, both of these excitation cases exert inferior control authority compared with ALE only excitation.

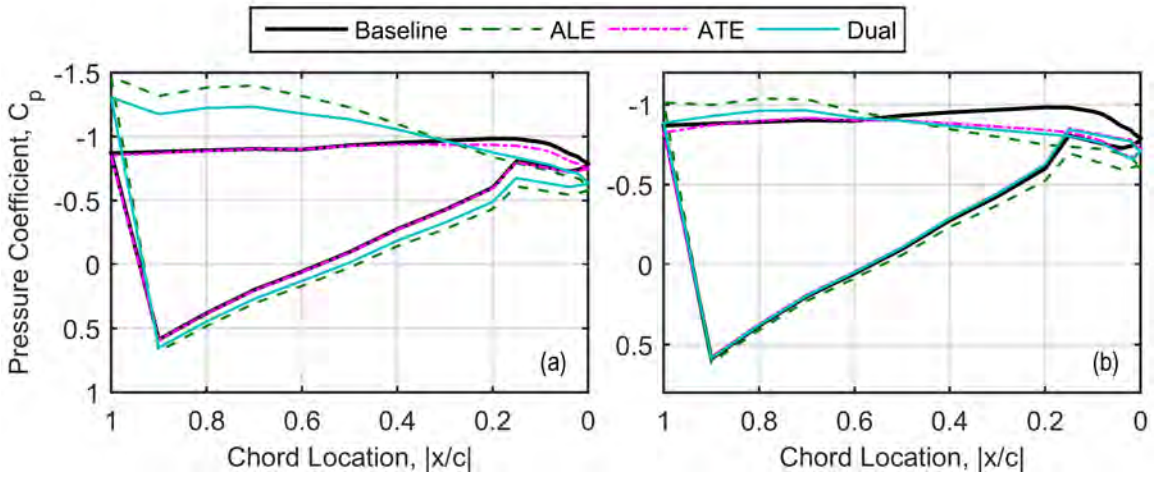

Figure 5.19: Surface static pressure distribution with (a) $St_F = 0.16$ and (b) $St_F = 0.89$, where ϕ_{ATE} for the synchronous excitation cases were 135° and 155°, respectively.

Synchronous excitation was predominantly characterized by the associated ALE excitation. Numerous combinations of excitation Strouhal numbers and phase delays were explored, but ALE excitation exerted total dominance in almost all cases. Two cases were found where ATE excitation in addition to ALE excitation had a significant effect: $St_F = 0.16$ with $\phi_{ATE} = 135°$ and $St_F = 0.89$ with $\phi_{ATE} = 155°$. In these two cases, the flow shares characteristics of individual excitation at the ALE and ATE. The resultant flow lies somewhere between the two independent excitations.

5.3.2 Asynchronous Excitation

Asynchronous operation, where each actuator operates at an independent frequency, is explore here. In this manner, the coherence in the wake may be diminished, rather than reinforced.

Surface static pressure data was acquired with asynchronous excitation. The static pressure curves are numerous and not interesting in their own right, so they have been

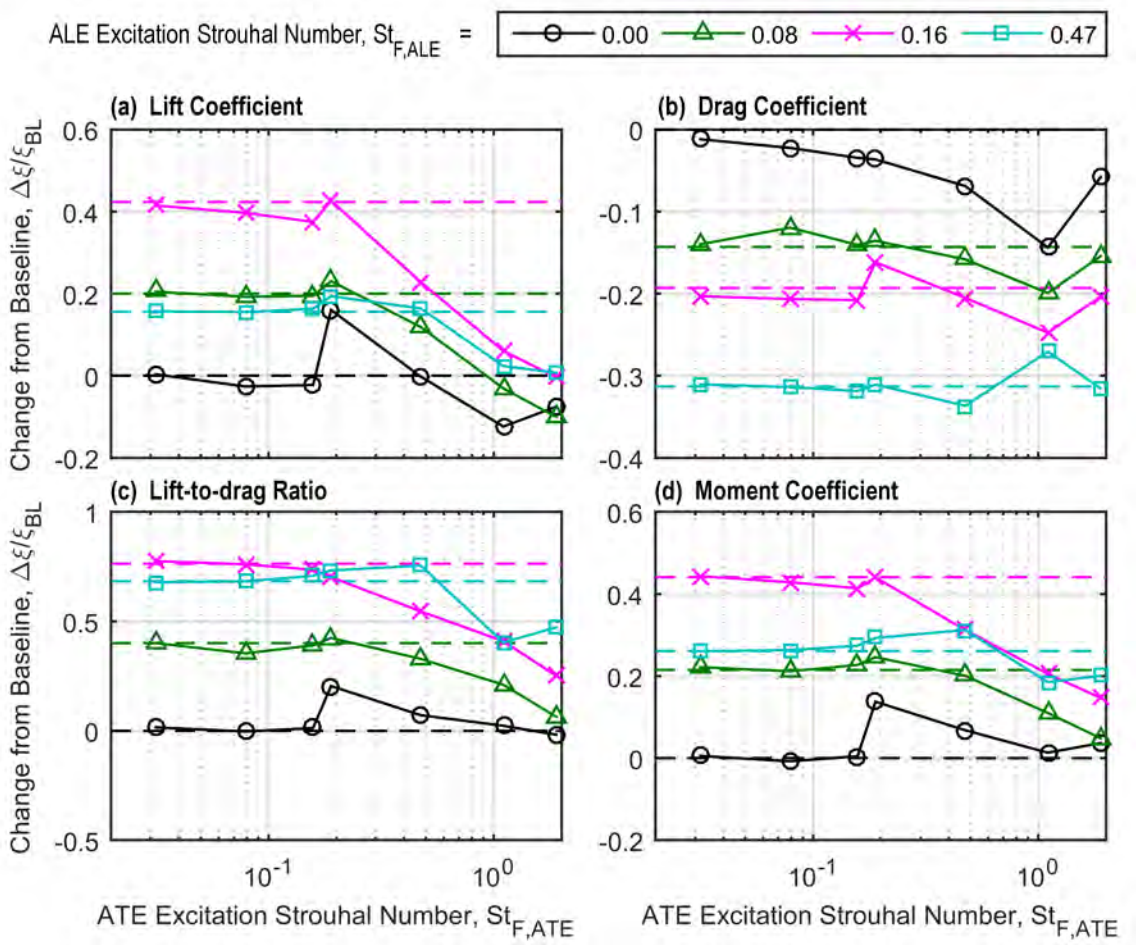

Figure 5.20: Changes in (a) sectional lift, (b) drag, (c) lift-to-drag, and (d) moment coefficients with asynchronous excitation.

reduced into four plots: change in lift, drag, lift-to-drag ratio, and moment, shown in Fig. 5.20(a–d). Each plot has four curves; each curve is a constant ALE excitation frequency and the x-axis is the ATE excitation frequency. The dashed lines represent ALE excitation only. The black line has an ALE frequency of zero, and is thus ATE excited only.

The overall trend is that the addition of ATE excitation counteracted the lift benefits of ALE excitation. As the ATE excitation increased, the amount of lift

decreased. For ALE excitation of 0.16 and 0.47, the lift decreased back to the baseline value. For ALE excitation of 0.08, the lift decreased beyond the baseline value and is close to the ATE only case. The effect on drag was surprisingly minimal. The change in drag curves are mostly horizontal (with the exception of the ATE only curve), suggesting that ALE excitation had a much more significant influence on drag than ATE excitation, even at high ATE frequencies. ALE excitation of $St_{F,ALE} = 0.47$ did benefit very slightly from moderate ATE excitation: the lift increased by a small amount and the drag decreased by a similarly small amount. At $St_{F,ALE} = 0.47$ and $St_{F,ATE} = 0.47$, the increase in lift-to drag ratio is 75% compared to 68% for ALE only excitation.

Chapter 6: Summary and Concluding Remarks

Flow control experiments were performed using NS-DBDs on a NACA 0015 airfoil in fully-reversed condition, which is anticipated to occur on the retreating blade side of advanced helicopters such as slowed-rotor compound rotorcraft. This symmetric airfoil, which is not typical of those used in rotorcraft blades, was used for simplification of an otherwise very complex problem. The Reynolds number based on chord length was fixed at $5.0 \cdot 10^5$. Two angles of attack were considered: $\alpha = 0°$ which is relevant to coaxial helicopters that may offload each rotor on the retreating blade side, and $\alpha = 15°$ which is relevant to helicopters with a single main rotor.

At $\alpha = 0°$, a small recirculation region formed behind the airfoil with symmetric regions of high vorticity on either side, similar to that of a flow behind a cylinder [18]. Alternating vortex shedding occurred at a Strouhal number of 0.12. A vast sweep of excitation frequencies was performed using a single actuator. However, there was no discernible influence upon the baseline behavior. Further optimizations were considered, but not employed. If a particular optimization were to exhibit superior control, it is theorized that a single actuator should also exhibit some degree of control. Since no control authority was observed, the exploration of these potential optimizations was unnecessary. Thus, it is concluded that NS-DBDs lack sufficient control authority in this configuration.

At $\alpha = 15°$, fully separated flow on the suction side extended well beyond the airfoil with naturally shed vortices at a Strouhal number of 0.19. Plasma actuation was evaluated at both the aerodynamic leading- and trailing-edge of the airfoil. Plasma actuation at the ALE generated organized coherent structures in the shear layer over the separated region. Moderate excitation had the most significant effects: creating moderately sized structures that convected far downstream, greatly reducing the separation area, increasing lift, and decreasing drag. Excitation at much higher Strouhal numbers resulted in the flow returning to its natural shedding state, but with less coherent structures that diffused in the wake. This reduced the separation area and significantly reduced drag. Plasma actuation at the ATE caused a reduction in the magnitude of the fundamental and harmonic peaks in pressure spectra over a broad range of excitation Strouhal numbers. Excitation at the ATE altered the structures over the separated region, suggesting an upstream communication. At excitation frequencies higher than the natural shedding frequency, the natural shedding process was disrupted, weakening the naturally shed structures in the wake. Synchronous excitation was predominantly characterized by the associated ALE excitation. Two cases were found where ATE excitation in addition to ALE excitation had a significant effect. In those two cases, the flow shared characteristics of individual excitation at the ALE and ATE. The resultant flow was somewhere between the two independent excitations. With asynchronous excitation, the addition of ATE excitation counteracted the lift benefits of ALE excitation. As the ATE excitation increased, the amount of lift decreased. The effect on drag was minimal, suggesting that ALE excitation has a much more significant influence on drag than ATE excitation, even at high ATE frequencies.

He *et al.* [56] investigated leading and trailing-edge flow control using AC-DBD actuators in both a steady and unsteady manner on a (conventionally oriented) NACA 0015 airfoil at $Re = 2.17 \cdot 10^5$ and $3.07 \cdot 10^5$. It is important to acknowledge that the mechanism behind AC-DBD excitation, which imposes a body force on the near-wall fluid and thus functions via momentum addition, differs fundamentally from NS-DBD excitation, which generates thermal perturbations capable of exciting instabilities [10]. Nonetheless, their findings with regard to unsteady excitation are still relevant. At the leading-edge, unsteady excitation resulted in the production of coherent vortical structures over the separated region [56], similar in nature to those of many others using plasma [10, 12, 30, 31] and synthetic jets [57–59]. Similar spanwise vortical structures are shown with the ALE excitation in Fig. 5.8 in the present work. However, since the NS-DBD excitation at the leading-edge excites natural flow instabilities to generate coherent spanwise vortices, the size and separation of the vortices are dependent on the excitation Strouhal number, as shown in Fig. 5.8. The flow responds to the excitation over a large range of Strouhal numbers. Even at low excitation Strouhal numbers, actuation caused the creation of coherent structures that convected downstream before the natural flow structure resumed. The mechanism responsible for this instability excitation is rapid Joule heating that creates nominally two-dimensional compression waves (both planar and cylindrical) [10].

He *et al.* [56] found no indication that unsteady forcing at the trailing-edge would be beneficial. However, the findings of Breuer and Jovičić [21] indicated that the flow past an inclined flat plate at $Re = 2.0 \cdot 10^4$ and $\alpha = 18^\circ$ is strongly dominated by the behavior of the trailing-edge vortex. Thus, adequate control of the trailing-edge vortex would influence the entire flow field. Although the Reynolds number of the

current work is much greater, the results shown in Figs. 5.15 and 5.16 demonstrate that ATE excitation had a direct influence upon both the ALE and ATE shear layers. The exact nature of the upstream communication is difficult to discern, as there are two likely candidates. The first and more probable candidate is that the perturbations from the ATE actuation could travel upstream toward the ALE shear layer origin via the separated region thus exciting instabilities at the ALE, but at reduced effectiveness due to the great distance between excitation and receptivity location. Alternatively, the alteration of the vortex formation at the ALE could come from the coupled nature of the shear layers: ATE excitation influences the ATE shear layer, which communicates to the wake-region of the ALE shear layer, which then communicates upstream to the ALE shear layer origin. Plogmann *et al.* [60] confirmed experimentally the existence of a global feedback loop in the wake of an airfoil at angle of attack. The feedback loop was found to be dominated by the boundary layer characteristics on the pressure side of the airfoil [60]. ATE excitation, which is on the pressure side of the airfoil, could therefore act as a boundary layer trip influencing the global feedback of the system.

Bibliography

[1] J. G. Leishman. *Principles of Helicopter Aerodynamics*. Cambridge University Press, 2nd edition, 2006.

[2] W. J. McCroskey. The phenomenon of dynamic stall. NASA Technical Memorandum 81264, NASA Ames Research Center, Moffet Field, CA, 1981.

[3] D. Walsh, S. Weiner, K. Arifian, A. Bagai, T. Lawrence, and R. Blackwell. Development testing of the Sikorsky X2 Technology^{TM} Demonstrator. In *American Helicopter Society 65th Annual Forum*, Grapevine, TX, May 27–29 2009.

[4] P. Roesch. Fast hybrid helicopter with long range with longitudinal trim control, September 2010.

[5] P. Eglin. Drive control and regulation method and system for a hybrid helicopter, December 2010.

[6] A. Datta, H. Yeo, and T. R Norman. Experimental investigation and fundamental understanding of a slowed UH-60A rotor at high advance ratios. In *American Helicopter Society 67th Annual Forum*, Virginia Beach, VA, May 3–5 2011.

[7] M. Potsdam, A. Datta, and B. Jayaraman. Computational investigation and fundamental understanding of a slowed UH-60A rotor at high advance ratios.

In *American Helicopter Society 68th Annual Forum*, Grapevine, TX, May 1–3 2012.

[8] Sikorsky. The added horizontal surface can be seen on the tail of the X2. Online via WIRED, June 2011. URL `http://www.wired.com/images_blogs/autopia/2011/06/10s4458-129.jpg`.

[9] Airbus Helicopters. Vehicles Eurocopter X3. Online via Wallpaperest, May 2014. URL `http://wallpaperest.com/wallpapers/vehicles-eurocopter-x3_393287.jpg`.

[10] J. Little, K. Takashima, M. Nishihara, I. Adamovich, and M. Samimy. Separation control with nanosecond-pulse-driven dielectric barrier discharge plasma actuators. *AIAA Journal*, 50(2):350–365, 2012. doi:10.2514/1.J051114.

[11] M. Samimy, J.-H. Kim, J. Kastner, I. Adamovich, and Y. Utkin. Active control of high-speed and high-Reynolds-number jets using plasma actuators. *Journal of Fluid Mechanics*, 578(1):305–330, 2007.

[12] C. Rethmel, J. Little, K. Takashima, A. Sinha, I. Adamovich, and M. Samimy. Flow separation control using nanosecond pulse driven DBD plasma actuators. *International Journal of Flow Control*, 3(4):213–232, 2011.

[13] Sikorsky X2 hits 250kt goal, 2010.

[14] A. Bagai. Aerodynamic design of the X2 Technology Demonstrator^{TM} main rotor blade. In *64th Annual Forum of the American Helicopter Society*, Montreal, Canada, April 29–May 1 2008.

[15] C. DuBois. Flow control on an airfoil under reversed flow condition using nanosecond dielectric barrier discharge actuators. Master's thesis, The Ohio State University, 2013.

[16] J. H. Gerrad. The mechanics of the formation region of vortices behind bluff bodies. *Journal of Fluid Mechanics*, 25(401), 1966.

[17] Jr. Oertel, H. Wake behind blunt bodies. *Annual Review of Fluid Mechanics*, 22:539–564, 1990. doi:10.1146/annurev.fl.22.010190.002543.

[18] C. H. K. Williamson. Vortex dynamics in the cylinder wake. *Annual Review of Fluids Mechanics*, 28:477–539, January 1996. doi:10.1146/annurev.fl.28.010196.002401.

[19] A. Roshko. Experiments on the flow past a circular cylinder at very high Reynolds number. *Journal of Fluid Mechanics*, 10(3):345–356, 1961. doi:10.1017/S0022112061000950.

[20] J. Zhang, N.-S. Liu, and X.-Y. Lu. Route to a chaotic state in fluid flow past an inclinded flat plate. *Physical Review E: Statistical, Nonlinear, and Soft Matter Physics*, 79(4), 2009. doi:10.1103/PhysRevE.79.045306.

[21] M. Breuer and N. Jovičić. Separated flow around a flat plate at high incidence: An LES investigation. *Journal of Turbulence*, 2(18), 2001. doi:10.1088/1468-5248/2/1/018.

[22] J. M. Chen and Y.-C. Fang. Strouhal number of inclined flat plates. *Journal of Wind Engineering and Industrial Aerodynamics*, 61:99–112, 1966.

[23] A. H. Lind, J. N. Lefebvre, and A. R. Jones. Time-averaged aerodynamics of sharp and blunt trailing-edge static airfoils in reverse flow. *AIAA Journal*, 52 (12):2751–2764, December 2014. doi:10.2514/1.J052967.

[24] A. H. Lind and A. R. Jones. Vortex shedding from airfoils in reverse flow. *AIAA Journal*, 2015. doi:10.2514/1.J053764.

[25] J. Kim and H. Choi. Distributed forcing of flow over circular cylinder. *Physics of Fluids*, 17, 2005. doi:10.1063/1.1850151.

[26] H. Choi, W.-P. Jeon, and J. Kim. Control of flow over a bluff body. *Annual Review of Fluid Mechanics*, 40:113–139, January 2008. doi:10.1146/annurev.fluid.39.050905.110149.

[27] T. C. Corke, C. L. Enloe, and S. P. Wilkinson. Dielectric barrier discharge plasma actuators for flow control. *Annual Review of Fluid Mechanics*, 42:505–529, January 2010. doi:10.1146/annurev-fluid-121108-145550.

[28] R. Dawson and J. Little. Characterization of nanosecond pulse driven dielectric barrier discharge plasma actuators for aerodynamic flow control. In *6th AIAA Flow Control Conference*, number 2012-3236, New Orleans, LA, June 25–28 2012.

[29] J. Poggie, N. J. Bisek, I. V. Adamovich, and M. Nishihara. Numerical simulation of a nanosecond pulse discharge in Mach 5 flow. In *51st AIAA Aerospace Sciences Meeting*, number 2013-0458, Grapevine, TX, January 7–10 2013.

[30] I. V. Adamovich, J. Little, K. Takashima, and M. Samimy. Nanosecond pulse surface discharge for high-speed flow control. In *6th AIAA Flow Control Conference*, number 2012-3137, New Orleans, LA, June 25–28 2012.

[31] R. Dawson and J. Little. Parametric investigation of nanosecond pulse driven dielectric barrier discharge plasma actuators for aerodynamics flow control. In *51st AIAA Aerospace Sciences Meeting*, number 2013-0398, Grapevine, TX, January 7–10 2013.

[32] S. Bhattacharya and A. Ahmed. Control of cylinder wake using three dimensional disturbances. *International Journal of Flow Control*, 2(1):61–72, March 2010. doi:10.1260/1756-8250.2.1.61.

[33] S. Bhattacharya and J. Gregory. Effect of three-dimensional plasma actuation on the wake of a circular cylinder. *AIAA Journal*, 53(4):958–967, April 2015. doi:10.2514/1.J053316.

[34] S. Bhattacharya and J. Gregory. Investigation of the cylinder wake under spanwise periodic forcing with a segmented plasma actuator. *Physics of Fluids*, 27 (014102), 2015. doi:10.1063/1.4905536.

[35] N. Nishioka and H. Sato. Measurements of velocity distributions in the wake of a circular cylinder at low Reynolds numbers. *Journal of Fluid Mechanics*, 65(97), 1974.

[36] P. K. Stansby. The effect of end plate on the base pressure coefficinet of a circular cylinder. *Aeronautical Journal*, 78(36), 1974.

[37] P. W. Bearman. Investigation of the flow behind a two-dimensional model with a blunt trailing edge fitted with splitter plates. *Journal of Fluid Mechanics*, 21 (241), 1965.

[38] A. Roshko. On the wake and drag of bluff bodies. *Journal of the Aeronautical Sciences*, 22(124), 1955.

[39] H. Sakamoto and H. Haniu. Optimum suppression of fluid forces acting on a circular cylinder. *Journal of Fluids Engineering*, 116(221), 1994.

[40] C. Dalton, Y. Xu, and J. C. Owen. The suppression of lift on a circular cylinder due to vortex shedding at moderate Reynolds numbers. *Journal of Fluids and Structures*, 15(617), 2001.

[41] C. J. Wood. The effect of base bleed on a periodic wake. *Journal of the Royal Aeronautical Society*, 68(477), 1964.

[42] P. W. Bearman. The effect of base bleed on the flow behind a two-dimensional model with a blunt trailing edge. *Aeronautical Quarterly*, 18(207), 1967.

[43] C. Min and H. Choi. Suboptimal feedback control of vortex shedding at low Reynolds numbers. *Journal of Fluid Mechanics*, 401(123), 1999.

[44] J. Little. *High-Lift Airfoil Separation Control with Dielectric Barrier Discharge Plasma Actuators*. Mechanical engineering, The Ohio State University, Columbus, 2010.

[45] M. Stanislas, K. Okamoto, C. Kähler, J. Westerweel, and F. Scarano. Main results of the third international PIV challenge. *Experiments in Fluids*, 45(1), 2008. doi:10.1007/s00348-008-0462-z.

[46] R. J. Adrian, K. T. Christensen, and Liu Z.-C. Analysis and interpretation of instantaneous turbulent velocity fields. *Experiments in Fluids*, 29(3):275–290, September 2000. doi:10.1007/s003489900087.

[47] K. K. Ahuja. Some unique experiments on receptivity. In *Shear Flow Control Conference*, number 85-0533, 1985. doi:10.2514/6.1985-533.

[48] D. W. Bechert. Excitation of instability waves in free shear layers, part 1, theory. *Journal of Fluid Mechanics*, 186:47–62, 1988. doi:10.1017/S0022112088000035.

[49] D. W. Bechert and B. Stahl. Excitation of instability waves in free shear layers, part 2, experiments. *Journal of Fluid Mechanics*, 186:63–84, January 1988. doi:10.1017/S0022112088000047.

[50] M. F. Barone and S. K. Lele. Receptivity of the compressible mixing layer. *Journal of Fluid Mechanics*, 540:301–335, October 2005. doi:10.1017/S0022112005005884.

[51] R. Ely and J. Little. Mixing layer excitation by dielectric barrier discharge plasma actuators. In *51st AIAA Aerospace Sciences Meeting*, number 2013-1012, January 7–10 2013. doi:10.2514/6.2013-1012.

[52] R. Ely and J. Little. The mixing layer perturbed by dielectric barrier discharge. In *43rd AIAA Fluid Dynamics Conference*, number 2013-2753, San Diego, CA, June 24–27 2013. doi:10.2514/6.2013-2753.

[53] A. P. Broeren and M. B. Bragg. Flow measurements over an airfoil during natural low-frequency oscillations near stall. *AIAA Journal*, 37(1), 1999. doi:10.2514/2.678.

[54] M. B. Bragg and D. C. Heinrich. Low-frequency oscillation over airfoils near stall. *AIAA Journal*, 31(7):1341–1343, 1993. doi:10.2514/3.49069.

[55] A. Sinha, H. Alkandry, M. Kearney-Fischer, and M. Samimy. The impulse response of a high-speed jet forced with localized arc filament plasma actuators. *Physics of Fluids*, 24(12), 2012. doi:10.1063/1.4772191.

[56] C. He, T. C. Corke, and M. P. Patel. Plasma flaps and slats: An application of weakly ionized plasma actuators. *Journal of Aircraft*, 46(3), 2009. doi:10.2514/1.38232.

[57] D. Weaver, K. W. McAlister, and J. Tso. Suppression of dynamic stall by steady and pulsed upper-surface blowing. NASA Technical Paper 3600, NASA Ames Research Center, Moffet Field, CA, February 1996.

[58] J.-Z. Wu, Z.-Y. Lu, A. G. Denny, M. Fan, and J.-M. Wu. Post-stall flow control on an airfoil by local unsteady forcing. *Journal of Fluid Mechanics*, 371:21–58, 1998. doi:10.1017/S0022112098002055.

[59] S. Hahn and D. You. Flow separation control over a pitching airfoil using an oscillatory jet. In *Proceedings of the Summer Program 2006*, pages 469–480. Center for Turbulence Research, 2006.

[60] B. Plogmann, A. Herrig, and W. Würz. Experimental investigation of a trailing edge noise feedback mechanism on a NACA 0012 airfoil. *Experiments in Fluids*, 54(1480), 2013. doi:10.1007/s00348-013-1480-z.